Interfacial Model Deciphering High-Voltage Electrolytes for High Energy Density, High Safety, and Fast-Charging Lithium-Ion Batteries

Yeguo Zou,† Zhen Cao,† Junli Zhang, Wandi Wahyudi, Yingqiang Wu, Gang Liu, Qian Li, Haoran Cheng, Dongyu Zhang, Geon-Tae Park, Luigi Cavallo, Thomas D. Anthopoulos, Limin Wang, Yang-Kook Sun,* Jun Ming**

Y. Zou, Dr. Y. Wu, G. Liu, H. Cheng, Dr. Q. Li, D. Zhang, Prof. L. Wang, Prof. J. Ming
State Key Laboratory of Rare Earth Resource Utilization, Changchun Institute of Applied Chemistry, CAS, Changchun 130022, China
E-mail: jun.ming@ciac.ac.cn

Y. Zou, G. Liu, H. Cheng, D. Zhang, Prof. L. Wang, Prof. J. Ming
University of Science and Technology of China
Hefei 230026, China

Dr. Z. Cao, Dr. W. Wahyudi, Prof. L. Cavallo, Prof. T. D. Anthopoulos
Physical Science and Engineering Division (PSE), King Abdullah University of Science and Technology (KAUST), Thuwal, 23955-6900, Saudi Arabia

Prof. J. Zhang
Key Laboratory of Magnetism and Magnetic Materials of the Ministry of Education, School of Physical Science and Technology, Lanzhou University, Lanzhou 730000, China
E-mail: zhangjl@lzu.edu.cn

G. T. Park, Prof. Y. K. Sun
Department of Energy Engineering, Hanyang University
Seoul 133-791, Republic of Korea
E-mail: yksun@hanyang.ac.kr

†These authors contributed equally

Keywords: Lithium-ion battery, high-voltage electrolyte, solvation structure, electrolyte/electrode interface, fast charging

Abstract

High-voltage lithium-ion batteries (HV-LIBs) enabled by high voltage electrolytes can effectively boost the energy density and power density, of which critical requirements to achieve long travel-distance, fast-charging, and reliable safety performances for electric vehicles. However, operating the batteries beyond the typical conditions of LIBs (4.3 V vs. Li/Li^+) leads to a severe electrolyte decomposition, while the interfacial side reactions remain elusive. These critical issues become the bottleneck for developing electrolytes for applications

in extreme conditions. Herein, we present an additive-free electrolyte that affords a high stability at high voltage (4.5 V vs. Li/Li^+), lithium-dendrite free features upon fast-charging operations (e.g., 162 mAh g^{-1} at 3 C), and superior long-term battery performances at low-temperature. More importantly, we introduce a new solvation structure-related interfacial model, incorporating the molecular-scale interactions between the lithium-ion, anion, and solvents at the electrolyte-electrode interfaces to interpret the battery performance. This report is a pioneering study to explore the dynamic mutual-interaction interfacial behaviors on the lithium layered oxide cathode and graphite anode simultaneously in the battery. Our molecular interaction model enables us to reveal new insights into electrode performances that differs from the known solid electrolyte interphase approach, and sets a new guideline to design versatile electrolytes for metal-ion batteries.

1. Introduction

Lithium-ion batteries (LIBs) have become an indispensable energy storage technology and played an important role in handheld electronics and electric vehicles.[1] However, the current LIBs cannot satisfy the growing demands for higher energy density, greater power capability, and better safety performances required for large-scale applications.[2] Although the high-capacity and/or high-voltage cathodes (e.g., Ni-rich, Li-rich layered oxides,[3] spinel LNMO cathodes[4]) as well as the high-capacity anodes (e.g., Li,[5] Si,[6] Sn[7] based materials) are being widely explored, the issue of developing a compatible electrolyte for these electrodes has become ever more important.[8] Particularly in extreme conditions (e.g., high-voltage, low/high temperature, super-fast charging/discharging, etc.), the detrimental electrolyte-electrode side reactions are inevitable because the electrolyte-determined interfacial stability as a precondition for battery operations is still yet fully understood.[9] For example, a severe electrolyte decomposition occurs on the surface of electrodes upon charging LIBs at a high voltage (≥4.5 V vs. Li/Li^+).[10] To this end, designing the electrolytes by stabilizing the electrolyte-electrode

interfaces has attracted great attention to enable boosting the high energy density, fast-charging time, and high-power density batteries.

Unfortunately, the conventional ethylene carbonate (EC)-based electrolytes are oxidized on the highly active surface of cathodes upon battery operation at high potential (≥4.3V vs. Li/Li^+).[11] EC was found to react with the singlet oxygen that was released from the NCM cathode,[12] and/or bring a transfer of atomic hydrogen from EC.[13] Thus, a numerous effort has been devoted to the development of electrolytes without using the EC solvent, such as super-concentrated[14], localized high-concentration electrolytes (LHCEs)[15], and all-fluorinated electrolytes[16]. Improved battery performances upon the use of these new electrolyte systems are mainly ascribed to the formation of robust cathode-electrolyte interface (CEI) film that helps to suppress the electrolyte decomposition. This viewpoint is similar as adding film-forming additives (e.g., vinylene carbonate (VC), prop-1-ene-1,3-sultone (PES) and triallyl phosphate (TAP)) in EC-free electrolytes.[17] However, the molecular-scale interactions of lithium-ion (Li^+), anion, and solvent on the electrolyte-electrode interfaces are not fully understood, while their effects on the Li^+ transports, electrochemical stability of the electrolyte, and the electrode performance also remain elusive. Therefore, to the best of our knowledge, there is no clear guideline from the aspect of interfacial chemistry for designing the electrolytes to improve the battery performances, besides the well-known consensus of CEI formation.

Lacking of a clear guideline (i.e., only focus on addressing the challenges on the cathode) has brought new problems into the anode. Many overlooked problems on the anode have been reported when the EC solvent-free strategy is employed to avoid the electrolyte oxidation on the cathode. For example, serious side-effects of severe decay of cycle performance and safety issues of LIBs have been reported upon the use of the EC-free electrolyte,[18] because the lithium metal is plated on the graphite anode readily during the fast charging or high-rate cycling due to the absence of EC solvent. Thus, an in-depth understanding of molecular-scale interfacial

behaviors and reaction mechanisms on the surface of electrodes, particularly the cathode and anode simultaneously, is crucial for developing electrolytes.

Herein, we report that a new carbonate-based high-voltage electrolyte employing a mixture of ethyl methyl carbonate (EMC) and methyl acetate (MA) solvents without adding any additive. The electrolyte successfully achieves excellent stability, fast-charging capability, and superior low-temperature performances of LIBs under a normal concentration of 1.2 M $LiPF_6$. We confirm that the interactions between the lithium-ion, anion, and solvent play a critical role to determine the interfacial behaviors between the electrolyte and electrodes. Based on our findings, we present a new interfacial model to explain the stability of the electrolyte on the surface of the NCM cathode and graphite anode. This work significantly complements our understanding of the solid electrolyte interphases (i.e., SEI, or CEI) effects on battery performances. More importantly, the presented interfacial model provides an efficient strategy to engineer the solid-liquid interfacial chemistry by regulating the solvation structure, which is crucial for a wide range of metal-ion battery systems.

2. Result and discussion

2.1 Features of high-voltage electrolyte

The newly-designed high-voltage electrolyte composes of EMC and MA solvents, in which EMC has a good oxidative stability (**Figure 1**a)[19] and MA has a low freezing point and a high ionic conductivity (**Figure 1**b).[20] While EMC can guarantee high electrolyte stability at high voltage, MA can overcome the disadvantages of EMC (i.e., low ionic conductivity and dielectric constant)[21] to enhance the ionic conductivity for greater rate capabilities, especially in the low-temperature conditions (**Figure 1**c). As a paradigm, the graphite || NCM622 battery employing our high voltage electrolyte (i.e., EMC/MA = 7/3 v/v, E/M73) demonstrates a high initial Coulombic efficiency (ICE) of 88.9% and a capacity of 201.2 mAh g^{-1}, which is close to that employing EMC electrolyte (89.7 %, 202.3 mAh g^{-1}) but much higher than that employing

MA electrolyte (72.3 %, 189 mAh g^{-1}) at the high voltage of 4.45 V (**Figure 1**d, see battery configuration in **Figure S1**). This result is consistent with the higher stability of the E/M73 electrolyte, as confirmed by the linear sweep voltammograms and stepwise potential sweep measurements[22] in **Figure S2.** Moreover, the comparative cycle performance of the cell employing different electrolytes also corroborates our observation (**Figure S3**a-c)

Besides, a high wettability of electrolytes also contribute to the power capacity of the cell. We find that the contact angle of E/M73 electrolyte on the NCM622 cathode, PP separator, and graphite anode are 9.1°, 30.6°, and 8.2°, respectively, which is lower than that of EMC (9.7°, 33.3°, and 9.4°) and E/E73 (i.e., the commercial electrolyte of 1.2 M $LiPF_6$ in EMC: EC=7:3 (v: v); 13.9°, 41.7°, and 12.8°) (**Figure S4**). This result should benefit from the low viscosity of MA solvent (i.e., 0.364 mPa·s). Then, a much higher power density can be obtained by employing the E/M73 electrolyte (**Figure 1**e). For example, the battery achieves a capacity of 175, 170, and 162 mAh g^{-1} at the rate of 2.0, 2.5, and 3.0 C, which is much higher than those employing EMC (i.e., 160, 145, and 137 mAh g^{-1}) and MA (i.e., 140, 119, and 93 mAh g^{-1}) electrolytes. The obtained initial discharge and power capacities are greatly improved compared to the high-voltage LIBs using different previously reported electrolytes (**Table S1**). Furthermore, the capacity is successfully retained to 197 mAh g^{-1} at 0.2 C after the high C-rate test, which is more improved than that of 176 mAh g^{-1} and 125 mAh g^{-1} by employing EMC and MA electrolytes, respectively. Moreover, we also confirmed that the cycle performance (i.e., capacity retention of 89.0% after 100 cycles at 1.9 mA cm^{-2}) and power capacity (i.e., 150.4 mAh g^{-1} at 3 C) are well-maintained even at a high mass loading of active materials (**Figure S3**d-e), demonstrating the practical capabilities of the electrolyte.

The fast-charging features of our electrolyte were further demonstrated by a fast CC-CC (Constant Current-Constant Current) protocol (**Figure 1**f). We find that 81.2 % of the initial capacity is achieved under 2.5 C (i.e., 24 min) using E/M73 electrolyte, of which value is higher

than 71.7% and 41.1% of the cells employing EMC and MA electrolytes. These criteria meet the fast-charging application standards stations well (e.g., 120 kW-Tesla Supercharger recharges 80% SOC in 40 min).[23] Moreover, our electrolyte retains 89.8% of the initial capacity at 0.5 C after 100 cycles under a low-temperature measurement of -5 °C, which is also much higher than that of 56.2 % and 13.4% obtained by EMC and MA electrolytes (**Figure 1**g). The results confirm the specialties of E/M73 high-voltage electrolyte, which enables a superior power capability and low-temperature performance at a high-voltage operation.

Note that the high-temperature performance deteriorated by the MA solvent is maximally suppressed by the EMC solvent in E/M73 electrolyte, where EMC has a positive effect likely additives.[24] The capacity retention of the cell is 85.4 % after 50 cycles at 1C when the cell was cycled at 50℃ (**Figure S3**c). The performance of the cell at high-temperature is even better than that employing the EMC electrolyte, while it is slightly reduced compared to that at room temperature (**Figure S3**b). This result should be mainly attributed to the change in the interaction between PF_6^- and Li^+ at high temperature, where PF_6^- is easier to reach the surface of the cathode and induce the solvent dehydrogenating. Detailed interpretation of this viewpoint is discussed in our interfacial model (section 2.7). Moreover, the thermal stability of the mixture of de-lithiated NCM622 cathode and electrolyte is studied by differential scanning calorimetry (DSC).[25] We find that the onset/peak temperature of the main peaks in the E/M73 electrolyte can be maintained at 219.9℃ / 238.1℃, which are much higher than 203.8℃ / 214.5℃ of the MA electrolyte and 217.7℃ / 222.5℃ of the commercial E/E73 electrolyte. The finding suggests that the thermal runaway reactions of the E/M73 electrolyte can be also suppressed at high potential likely in the EMC electrolyte (i.e., 253.3℃ / 255.7℃). The results demonstrate that the disadvantages of MA solvent could be overcome maximally by the EMC solvent from the aspects of bulk electrolyte and interfacial chemistry, as discussed later.

2.2 Electrode impedance analysis

The foundation of high performance of the electrolyte was investigated by the hybrid pulse power characterization (HPPC) and electrochemical impedance spectroscopy (EIS) measurements. The area-specific impedance (ASI) change of HPPC is the most direct technique to compare battery power characteristics (**Figure S5**).[26] The ASI values calculated by equation $R_{disc} = (V_0 - V_1) / I_{disc}$ and the corresponding depth of discharge (OCV) in different electrolytes are shown in **Figure 2**a-c. The average impedance of the full cell employing E/M73 electrolyte increased slightly from 59.9 Ω cm^2 to 64.4 Ω cm^2 after 5 HPPC cycles, while the corresponding values in the EMC and MA electrolytes increased from 75.4 Ω cm^2 to 82.2 Ω cm^2 and from 96.1 Ω cm^2 to 106.4 Ω cm^2, respectively. The finding demonstrates that the ohmic and concentration polarization are very low in the E/M73 electrolyte. Besides, the corresponding OCVs of the E/M73 electrolytes under various DODs were also the most stable compared to that of EMC and MA electrolytes (**Figure 2**a-c).

The EIS test was further employed to explore the interfacial impedance evolution of the full battery upon cycling (**Figure 2**d-f, **Table S2**). The R(Z) impedance of the full cell employing the EMC (94.7 Ω cm^2) and EM73 (92.2 Ω cm^2) electrolytes is similar after 200 cycles. In contrast, the value is higher in the full cell employing MA electrolytes (128.6 Ω cm^2) (**Figure 2**d), showing the same trend as their cycling performance (**Figure S3**b). The origins of the impedance were analyzed by the R(Z) impedance of the symmetric NCM622 ‖ NCM622 and graphite ‖ graphite cells. We find that the impedance of the symmetric NCM622 ‖ NCM622 cell using E/M73 electrolyte (176.8 Ω cm^2) is slightly higher than that using EMC electrolyte (166.6 Ω cm^2), which is much lower than that using MA electrolyte (267.3 Ω cm^2) (**Figure 2**e). This result demonstrates that EMC is more compatible with the cathode at high voltage, while the amount of MA needs to be controlled prudentially due to its low stability. More significant differences were observed on the cycled graphite anode. The R(Z) impedance of symmetric graphite ‖ graphite cells employing E/M73 electrolyte is about 14.4 Ω cm^2 after 200 cycles,

which value is much lower than 21.1 Ω cm^2 and 29.8 Ω cm^2 of that using EMC and MA electrolytes (**Figure 2**f), respectively. The result shows that the electrolyte decomposition on the graphite anode could be mitigated by E/M73 electrolyte. The impedance analysis shows that different electrolyte decomposition occurs on the surface of electrodes, giving rise to different SEI formations. However, the role of electrolyte compositions in the electrolyte decomposition that occurs on the surface of electrodes needs to be further studied at the molecular scale.

2.3 Electrolytes/cathode interface

The morphology and crystalline structure of the cycled NCM622 cathodes were investigated to understand the origin of different performances of the electrolytes (**Figure 3**). We find that the secondary particles are intact and distributed evenly on the cycled NCM622 electrodes when the EMC and E/M73 electrolytes were used (**Figure 3**a, a_1, and a_2). The only difference is a little depositions observed on the smooth surface of NCM622 particles cycled with the E/M73 electrolyte (**Figure 3**b, b_1 and b_2, **Figure S6**a). In contrast, microcracking in the secondary particles and more decomposition products are observed on the surface of the primary particles upon the use of MA electrolyte (**Figure 3**c, c_1, and c_2). The observation is consistent with the impedance analysis (**Figure 2**e), demonstrating the durability of the EMC solvent for the cathodes.

X-ray photoelectron spectroscopy (XPS) analysis further confirms the different components of decomposed electrolytes on the surface of NCM622 cathodes. There is a similar component of O-lattice (529.3 eV),[27] C=O (532 eV), and C-O groups (533.7 eV) [28] on the cathodes cycled with EMC and E/M73 electrolytes (**Figure 3**d). In contrast, the amount of C=O is dominant while the O-lattice is absent on the surface of cathode cycled with MA electrolyte (**Figure S7**a), which is because the MA solvent is decomposed to form lithium alkyl carbonates and carbonate salt readily and then covers the surface of the NCM622 cathode. Then, the signal

of O-lattice on the NCM622 might be covered so that the spectra are difficult to be detected. More information could be summarized from the F 1s spectra, in which the peaks at 687.8 eV, 686.6 eV, and 685.1 eV correspond to the PVDF binder,[10] $Li_xPO_yF_z$ (i.e., the decomposition products of $LiPF_6$),[27] and $LiM_xF_yO_z$ (M = Ni, Co, or Mn) (i.e., formed by reacting with HF),[29] respectively (**Figure 3**e). We find that the relative content of $LiM_xF_yO_z$ increased **(Figure S7**b) with increasing the volume of MA, which is due to the content of the HF (i.e., generated by reacting protic species from the dehydrogenation of solvents with $LiPF_6$) increased in the MA electrolyte. In other words, the dehydrogenation for solvents and the oxidative decomposition of $LiPF_6$ was suppressed in EMC and E/M73 electrolytes, thus the amount of $Li_xPO_yF_z$ in CEI becomes dominant compared to the $LiM_xF_yO_z$.

The crystallographic variation of the NCM622 cathodes was further analyzed by the peak shifts of (003) scattering angles in the XRD patterns (**Figure 3**f). The peak of (003) was shifted to a lower angle in the cathode cycled with the MA electrolyte, demonstrating the increased crystal plane cracks caused by the local structural collapse. This could be ascribed to the serious MA electrolyte decomposition, in which side reactions can corrode the electrode and cause structural degradation. The local structural change of the NCM622 cathode under the high-resolution transmission electron microscope (HRTEM) gives more evidence (**Figure 3**g-j), in which the layered (i.e., *R-3m* space group[30]) and partial spinel phases coexist in the inner and outer surface area on the NCM622 electrode cycled with the EMC electrolyte (**Figure 3**h_1-h_2). In contrast, the spinel phases increased slightly with the E/M73 electrolyte (**Figure 3**i_2), while the rock-salt phases (Ni-O)[31] could be also detected in the MA electrolyte (**Figure 3**j_3). The result demonstrates the necessity of adding EMC into MA to protect the NCM cathode, otherwise, the high-valence Ni^{4+} and Ni^{3+} ions formed in a fully charged state could be easily reduced to Ni^{2+} ions by MA. The highly active oxidative Ni^{4+} and electrolytes decomposition products, such as HF, could form an exceptionally unstable environment under the high-voltage

charge.[32] This process could trigger a severe oxygen evolution from the electrode, induce phase transformation, and further exacerbate the electrolyte decomposition.

2.4 Electrolytes/anode interface analysis

The interaction between the electrolyte and graphite anode is also important in the full batteries, especially during cycling at fast charging and high voltage. The variation in the cycled graphite anodes with different electrolytes was investigated in **Figure 4**. The lithium deposition and electrolyte decomposition are observed on the surface of cycled graphite using the EMC electrolyte (**Figure 4**a, d *vs.* **Figure S6**b). The findings are due to the high concentration polarization of EMC electrolytes and the reactivity between lithium metal and EMC solvent. In contrast, the lithium deposition and electrolyte decomposition on the surface of graphite anode were significantly mitigated by using the E/M73 electrolyte (**Figure 4**b, e). The results are consistent with the impedance analysis (**Figure 2**f). The observations of graphite cycled with the MA electrolyte lay intermediates between the EMC and E/M73 electrolytes (**Figure 4**c, f). The compatibility of electrolytes judged from the cycled graphite anodes is in the sequence of E/M73 > MA > EMC, which viewpoint was further proved by the stability in the symmetric Li || Li cells (**Figure S8**). These results demonstrate the necessity of MA added into the EMC electrolyte to pursue good compatibility with the graphite anode, which significantly suppresses lithium deposition and electrolyte decomposition. Although EMC demonstrates good compatibility with the NCM622 cathode at high voltage, EMC could react with fresh lithium readily on the graphite anode surface and cause severe capacity decay (**Figure S3**b).

Our observations was further confirmed by XPS analysis of the electrolyte decomposition products on the graphite anodes. The $LiCO_3$ peaks in C 1s spectra (i.e., 289.9 eV) [33] and Li 1s spectra (i.e., 55.3 eV vs. LiF at 56.0 eV) [34] significantly increase on the graphite cycled with the EMC electrolyte (**Figure 4**g, **Figure S7**c, d, f), suggesting an increased formation of Li_2CO_3 due to reaction between the deposited lithium metal and EMC solvent. This is consistent with

the result in O 1s spectra judged by C=O at 532.5 eV and the C-O groups at 533.7 eV [28] (**Figure 4**h, **Figure S7**e). Besides, F 1s spectra of the graphite anode cycled with EMC electrolyte shows a much stronger Li_xPF_y peak (i.e., at 688.3 eV [33]) than that of $Li_xPO_yF_z$ (i.e., at 686.6 eV [27]), but the LiF peak (i.e., at 685.0 eV [35]) is more obvious in comparison to the MA electrolyte (**Figure 4**i, **Figure S7**g). The result indicates that the decomposition of $LiPF_6$-species is more serious in EMC electrolytes but oxygen-containing organic decomposition products are mainly in the MA electrolytes. The relatively higher content of $LiCO_3$ and C-O on the surface of graphite anodes cycled with EMC and MA electrolytes than that with the E/M73 electrolyte further indicates the growth of carbon-oxygen-containing species (**Figure S7**f), such as the oligomers formed from the reduction of the electrolyte solvent by the deposited lithium metal. We have carried out sets of characterizations on the surface of NCM cathodes and graphite anodes, which corroborate the roles of the electrolyte composition on the decomposition products. Besides the composition and architecture characterizations of the electrolyte decomposition products, understanding the electrolyte decomposition process on the surface of the electrodes remains unclear, thus, a molecular-scale interfacial model of different electrolyte compositions is needed to interpret the details.

2.5 Role of solvation structure

The lithium-ion solvation structure was studied firstly by the Fourier transform infrared spectroscopy (FTIR). The combined peak at 1750 cm^{-1} and 1747 cm^{-1}, corresponding to the C=O stretch vibrations of EMC and MA, [11, 36] has a redshift and was split into two main peaks at 1718 cm^{-1} and 1712 cm^{-1} when the 1.2 M $LiPF_6$ salt was dissolved into the solvent mixture (**Figure 5**a, **Figure S9**a). This is a well-known solvation process, in which the ionic compound of Li^+-PF_6^- was solvated by the solvents, and then lithium-ion coordinates with the solvents to form a solvation structure through the Li^+-O interactions. Then, the solvated anion (PF_6^-) is classified into uncoordinated (free) PF_6^- (at 845 cm^{-1}) and Li^+--PF_6^- (i.e., contact ion pairs, CIPs)

at the peaks of 834 cm^{-1} and 870 cm^{-1}[37] (**Figure 5**b, **Figure S9**b). In particular, the coordinated number or proportion of each electrolyte species was quantitatively estimated by deconvoluting the FTIR spectra deliberately (**Figure 5**e, **Table S3**).[38]

We find that the coordination number of MA molecules (Li^+-MA) increases while that of the EMC molecules (Li^+-EMC) and CIPs ratio (Li^+--PF_6^-) decreases with increasing the volume of MA in the electrolyte. This observation is reasonable because MA has a higher capability to dissociate $LiPF_6$ due to its higher dielectric constant (i.e., ε_{MA} = 6.68) compared to EMC (i.e., ε_{EMC} = 2.958).[21] Thus, PF_6^- becomes hard to involve in Li^+-solvation structure when MA was added into the EMC electrolyte, which is further corroborated by the ^{7}Li-NMR and ^{19}F-NMR analysis of the electrolytes (**Figure 5**c-d, **Figure S9**). Firstly, the ^{7}Li-NMR chemical shift moves to the downfield (i.e., to higher values [39]) when MA was added into the EMC electrolyte to form E/M73. The downfield shift appears because MA participates in the coordination with Li^+ in the first solvation structure, which reduces the shielding effect on the Li^+ ions due to the low interaction strength of Li^+-MA (i.e., -44.72 Kcal mol^{-1} vs. -50.66 Kcal mol^{-1} for Li^+-EMC) (**Figure 5**i-j) and reduces the contact opportunity of Li^+ and PF_6^- due to the high dielectric constant of MA. The same phenomenon is observed in the chemical shift of ^{19}F-NMR where MA reduces the shielding effect on the Li^+ ions and effectively dissociates Li^+-PF_6^- coordination, which is consistent with the observation in FTIR. Based on our findings, the proposed coordination structures are illustrated in **Figure 5**f-h.

Note that the above analysis presented in **Figure 5**a-h is an average coordination structure for Li^+ and the solvent, while one Li^+ can coordinate with four solvent molecules in the electrolyte. EMC has a strong interaction with Li^+ in the solvation structure in the EMC electrolyte, and PF_6^- may contact with Li^+ in a high frequency due to the low dielectric constant, as demonstrated by the high CIP ratio (i.e., Li^+--PF_6^-) in FTIR (**Figure 5**f-h). In contrast, MA has a relatively weak interaction (vs. EMC) with Li^+ in the solvation structure, and PF_6^- is hard

to contact with Li^+ because of the high dielectric constant. Then, the appearance frequency of PF_6^- around the first solvation structure in the electrolyte decreases in the sequence of EMC> E/M73 > MA (i.e., $f_1 > f_3 > f_2$).

The Li^+-O radial distribution function (RDF) corroborates the different interactions between the solvents (e.g., EMC, MA) and Li^+ (**Figure 5**k). The Li^+-EMC coordination is stronger than that of Li^+-MA, which is consistent with the observed strong shielding effect and the chemical shift that appeared at the high-field in NMR (**Figure 5**c). The Li^+- PF_6^- RDF for PF_6^- neighbor to Li^+ also confirms the higher frequency of PF_6^- appeared around Li^+ in the EMC electrolyte than that in the MA electrolyte (**Figure 5**k). In brief, the MA solvent can dissociate $LiPF_6$ effectively and compete with the EMC solvent to participate in the first solvation structure around Li^+ when MA was added into the EMC electrolyte. Then, PF_6^- is easy to contact with Li^+ and form CIPs in EMC electrolytes (EMC and E/M73), but PF_6^- can be excluded out from the solvation structure by MA in the MA electrolytes. These results are consistent with the FTIR and NMR results.

As a result, the conductivity of electrolytes increases from 5.0 mS cm^{-1} to 21.7 mS cm^{-1} with increasing the amount of MA from 0% to 100% (**Figure 5**l). This is because EMC could be replaced by MA in the solvation structure, where PF_6^- could also keep far from Li^+ due to the higher dissociated capability and then demonstrate enhanced mobility of PF_6^-. In contrast, the transference number of Li^+ decreases from 0.443 to 0.336 with increasing the amount of MA, especially when the percentage volume of MA is more than 50 %. This is consistent with the increased mobility of PF_6^- (i.e., $t_+ + t_- = 1$) (**Figure 5**l, the calculation of t_{Li}^+ resulted from **Figure S10**).[40] These results are in good agreement with the change of CIPs ratio, in which the presence of PF_6^- was excluded from the solvation structure (i.e., the increased number of free PF_6^-). Note that although there is a high transference number in the EMC electrolyte, the very low conductivity of 5.0 mS cm^{-1} could cause the lithium metal deposition on the graphite

anode due to the severe concentration polarization (**Figure 4**a, d). While the E/M73 electrolyte has a suitable conductivity of 8.2 mS cm^{-1} and a transference number of 0.419, which can guarantee a good rate capability and lithium-dendrite-free fast charging features (**Figure 1**e-f, **Figure 4**b, e).

2.6 Simulation of electrolyte behavior

We investigated the Li^+-solvation structure in the bulk electrolyte to interpret the observed electrochemical performance in different electrolytes. Then, a solvation structure-related interfacial model can be constructed to interpret the root cause of the varied performance in the different electrolytes. Firstly, the electron distribution of the Li^+-solvent-PF_6^- complexes (i.e., CIPs) illustrated by electrostatic potential mapping was presented in **Figure 6**a. The active electrons of the Li^+-solvent-PF_6^- complexes increase with the increasing volume of MA solvent. This finding demonstrates that the high Coulombic interaction exists between PF_6^- and the positively charged cathode electrode when the volume of MA solvent is dominant in the electrolyte (e.g., the volume of MA > 50 %). Secondly, the desolvation energy of Li^+ was also considered to analyze the interaction between the Li^+-solvent-PF_6^- in different electrolytes (**Figure 6**b). We find that the Li^+ desolvation energy ($E_{Li^+\text{-}3MA\text{-}PF_6^-}$, -84.9 Kcal mol^{-1}, $E_{Li^+\text{-}2MA\text{-}EMC\text{-}PF_6^-}$, -92.41 Kcal mol^{-1}, or $E_{Li^+\text{-}MA\text{-}2EMC\text{-}PF_6^-}$, -97.39 Kcal mol^{-1}) was reduced when the volume of MA solvent is dominant in electrolyte compared to that of EMC ($E_{Li^+\text{-}3EMC\text{-}PF_6^-}$, -101.34 Kcal mol^{-1}). This implies that the Li^+-solvent-anion complexes interaction is much weaker in the presence of MA and E/M73 than that in EMC electrolyte, which could affect the Li deposition or Li^+ (de-)intercalation behavior at graphite.

Thirdly, the HOMO and LUMO energy of the solvent, solvent-PF_6^-, Li^+-solvent, and Li^+-solvent-PF_6^- complex are also presented in **Figure 6**c. We find that the oxidation stability of all solvents increases when the solvent coordinates to Li^+ (i.e., the HOMO energy of Li^+-solvent is lower than solvent), but the stability is weakened once the solvent coordination with PF_6^- (i.e.,

the HOMO energy of solvent-PF_6^- is higher than solvent or Li^+-solvent-PF_6^- is higher than Li^+-solvent). This is because the solvent-induced by PF_6^- can lose the electrons easier, and then the H-abstraction of solvent can occur at the high potential, forming the HF upon the cycling. Thus, making PF_6^- far from the solvent is important to maintain the electrolyte stability at the cathode interface, while the reduced ability of solvent, Li^+-solvent, and Li^+-solvent-PF_6^- must also be considered.

2.7 Interfacial Model

The electrolyte formula of $Li^+[solvent]_x[PF_6^-]$ (x, calculated by the molar concentration) was used to describe the electrolyte-electrode interfacial behaviors.[41] For example, 1.2 M $LiPF_6$ solvation in the EMC, E/M73 and MA electrolytes are described as $Li^+[EMC]_{8.11}[PF_6^-]$, $Li^+[MA]_{3.14}[EMC]_{5.68}[PF_6^-]$ and $Li^+[MA]_{10.46}[PF_6^-]$, respectively. Then, the interfacial model was derived when Li^+ was de-solvated from the solvation structure. The relative frequency of PF_6^- around the Li^+ solvation structure in the bulk electrolytes and at the electrolyte-electrode interfaces is presented in **Figure 7**. Different interfacial behaviors of the electrolytes and their relations with the electrode performances are discussed in detail later.

In the EMC electrolyte, PF_6^- appears around Li^+ in the solvation structure with a high frequency (i.e., f_1) due to the low dielectric constant of EMC (i.e., the high CIPs ratio) in the EMC electrolyte. A strong interaction (i.e., f_1') exists between Li^+ and EMC-PF_6^-, which such interaction weakens the Coulombic interaction between PF_6^- and the positively charged cathode (**Figure 7**a). In this state, the EMC-PF_6^- pair is difficult to move closer towards the surface of the cathode due to the weak interaction. As a result, EMC-PF_6^- is also hard to be oxidized due to the difficulty in transferring electrons to the cathode and the high oxidation stability (*vs.* MA-PF_6^-). Besides, the oxidation stability of free EMC solvent is also improved, because the free EMC coordinates with Li^+ when Li^+ is extracted from the cathode upon charging process to form the Li^+-EMC pair (i.e., the HOMO energy of Li^+-EMC was lower than free EMC) (**Figure**

6c). Particularly, PF_6^- is also difficult to be de-solvated in the initial Li^+ solvation structure and then moves closer to the newly formed Li^+-EMC pair (i.e., the less free PF_6^- can move close to the Li^+-EMC pair as most of PF_6^- bounds to around Li^+ and solvent in the bulk electrolyte due to the high CIPs ratio). Thus, the detrimental effect of PF_6^- reaction with EMC solvent that produces HF could be effectively mitigated. In this EMC electrolyte system, EMC-PF_6^- and EMC could be well-stabilized even at a high charge voltage condition; however, the low ionic conductivity of the EMC electrolyte gives rise to a low-rate capacity (**Figure 1**e-f).

In contrast, the solvation structure in the MA electrolyte shows PF_6^- with a low frequency that appears around Li^+ (i.e., f_2) in the solvation structure due to the high dielectric constant of MA (i.e., the low CIPs ratio) in the MA electrolyte (**Figure 7**b). Thus, the MA-PF_6^- pair demonstrates a weak interaction with Li^+ (i.e., f_2'), then the MA-PF_6^- can moves closer to the cathode surface due to the strong Coulombic interaction between PF_6^- and the positively charged cathode. As a result, the electron transfer from MA-PF_6^- to the cathode is possible, leading to a lower oxidation stability of MA-PF_6^- compared to that of EMC-PF_6^-. Note that the oxidation stability of the free MA solvent is not improved, as the case is opposite in the EMC electrolyte, because PF_6^- can be de-solvated from the initial Li^+ solvation structure readily and then moves closer towards the newly formed Li^+-MA pair. The free PF_6^- can move closer towards the formed Li^+-MA as most of PF_6^- is not bound with Li^+ and solvents in the bulk electrolyte (i.e., the low CIPs ratio)), when Li^+ was extracted from the cathode. As a result, PF_6^- promotes the oxidation of Li^+-MA easier on the cathode surface, as judged by the HOMO of Li^+-MA and Li^+-MA-PF_6^- (**Figure 6**c), leading to a severe decomposition of the MA electrolyte on the cathode surface.

In the E/M73 electrolyte, MA solvent participates in the first solvation structure, where partial MA can involve in the dissociation of Li^+-PF_6^- because of insufficient EMC (i.e., $Li^+[MA]_{3.14}[EMC]_{5.68}[PF_6^-]$). The analysis is consistent with the observed medium CIPs ratio

in the E/M73 electrolyte. PF_6^- has a medium frequency (i.e., f_3) that appeared around Li^+, which value is higher than that in the EMC electrolyte (i.e., $f_1 < f_3$) but lower than that in the MA electrolyte (i.e., $f_3 < f_2$) (**Figure 5**f-h). Then, PF_6^- demonstrates a medium interaction with the Li^+-solvent in the E/M73 electrolyte compared to those in the EMC and MA electrolytes (i.e., $f_1' < f_3' < f_2'$), giving rise to a medium Coulombic interaction and a safe distance between the PF_6^- and the positively charged cathode (**Figure 7**c). As a result, the MA-PF_6^- pair is hard to be oxidized due to the difficulty in transferring electrons to the cathode and also has high oxidation stability (i.e., MA is close to Li^+ but far from PF_6^-). This phenomenon is similar to that in the EMC electrolyte. Moreover, the EMC solvent can also prevent PF_6^- moving closer to the Li^+-MA pair at the surface of the cathode when Li^+ was extracted from the cathode. Our conjecture was further corroborated by the simulations, where the frequency of PF_6^- appears around the surface of the cathode is in the sequence of EMC < E/M73 < MA electrolytes (**Figure 7**a'-c'). These results demonstrate the importance of solvent to determine the stability of electrolytes on the surface of the cathode at high potential.

Our interfacial model was also well-constructed on the surface of graphite anode. In the EMC electrolyte, Li^+ could interact with PF_6^- via strong binding energy and high frequency (i.e., f_1) due to the low dielectric constant of EMC (**Figure 5**f), giving rise to high de-solvation energy (**Figure 6**b). Thus, lithium dendrite is easy to be plated on the graphite anode because of the resultant high polarization. This process is detrimental because lithium can react with the EMC solvent due to less reduction stability of the Li^+-EMC pair.[42] Our finding not only interprets the observed lithium on the graphite anode in **Figure 4**a but also explains the root cause of the reduced cycling stability of the battery in the EMC electrolyte (**Figure S3**b). Note that some side-reaction products can be observed in the MA electrolyte resulting in the less formation of lithium dendrite, which is attributed to a low Li^+ de-solvation energy (**Figure 6**b) and the by-effect of the polarization is less than that in the EMC electrolyte (weaker interaction between

Li^+ and MA solvent or anion in **Figure 5**g, j). On the other hand, the side-reaction between lithium dendrite and MA is a serious issue, which is because the LUMO energy of MA electrolyte is low (**Figure 6**c). Thus, decomposition products of the electrolyte were observed at the graphite anode. The finding further demonstrates that although the single MA solvent can regulate the intercalation or deposition of Li^+ by reducing the polarization, the high reduction activity would lead to the decay of the battery.

Interestingly, we have found a completely different interfacial behavior in the E/M73 electrolyte. First, the interaction between EMC and Li^+ is weakened by the MA solvent, where PF_6^- could also keep far from Li^+ compared to that in the EMC electrolyte. Then, Li^+ de-solvation becomes easier, under which the intercalation of Li^+ into graphite anode is preferable compared to formation of lithium dendrite. Moreover, the reduction stability of E/M73 could be improved further because the EMC solvent can compete with MA in the Li^+ solvation structure. Thus, the E/M73 electrolyte has the combined advantages of EMC and MA electrolytes, thereby demonstrating better stability without formation of lithium dendrite and enabling a good cycling performance of the battery. Note that our conjecture was further corroborated by the simulations, where the MA solvent could change the interfacial behaviors (i.e., Li^+-solvent-anion interactions) when the MA was added into EMC electrolyte for form E/M73 (**Figure 7**d'-f').

To this end, for the first time, we have constructed dynamic mutual-interaction interfacial behaviors on the surface of the cathode and anode simultaneously. The varied electrolyte-electrode behaviors (i.e., the behaviors of Li^+-solvent-anion pairs) were thoroughly studied by experiments (e.g., FTIR, NMR, etc.) and simulations, which enable us to unravel the relationship between the interfacial behaviors and the electrode performance. This breakthrough will advance the development of battery electrolytes. To date, numerous simulations have been devoted to exploring the properties of electrolytes, which covers the

study on stability and decomposition routines of electrolytes, as well as variation in the Li^+ solvation structure from bulk electrolytes to electrode interfaces.[43] However, to our knowledge, there is no report on interfacial models to elucidate the relationships between the interfacial behaviors and the electrode performances. Based on our results, we believe that the interfacial interaction is a significant factor that affects the battery performance, of which at least the interfacial interactions is similarly important as the role of SEI/CEI.[44] Our discovery provides a new view-angle to understand the electrolyte-electrode interactions and then efficiently improve the battery performance, prompting the development future batteries with diverse systems. Therefore, development of knowledge in the effect of SEI/CEI and the electrolyte-electrode interfacial interactions (i.e., the behaviors of Li^+-solvent-anion pair) should be kept in balance simultaneously upon designing future electrolytes.

3. Conclusion

A new high-voltage electrolyte employing a co-solvent strategy without any additive has been demonstrated, showing a fast-charging capability of LIBs with an excellent long-term cycle performance, high-power stability, and lithium-dendrite free electrodes. More importantly, a pioneering interfacial model related to the Li^+ solvation structure is presented both on the cathode and anode, which unravels the molecular-scale of Li^+-solvent-anion interactions on the surface of the electrodes as well as their roles in the battery performances. Our interfacial model elucidates a new view-angle to understand the key relationships of Li^+ solvation structure in the electrolyte and the performance of electrodes, paving the way to a hitherto undiscovered guideline for designing electrolytes for metal-ion batteries.

Supporting Information

Supporting Information is available from the Wiley Online Library or from the author.

Acknowledgments

This work is supported by the National Natural Science Foundation of China (21978281, 21975250, 11974150) and the National Key R&D Program of China (2017YFE0198100). The authors also thank the Independent Research Project of the State Key Laboratory of Rare Earth Resources Utilization (110005R086), Changchun Institute of Applied Chemistry, Chinese Academy of Sciences. The research was also supported by King Abdullah University of Science and Technology (KAUST) and Hanyang University. The computational work was done on the KAUST supercomputer.

Received: ((will be filled in by the editorial staff))
Revised: ((will be filled in by the editorial staff))
Published online: ((will be filled in by the editorial staff))

References

[1] a)J. M. Tarascon, M. Armand, *Nature* **2001**, *414*, 359; b)B. Scrosati, J. Hassoun, Y.-K. Sun, *Energy Environ. Sci.* **2011**, *4*, 3287; c)M. Li, J. Lu, Z. Chen, K. Amine, *Adv. Mater.* **2018**, *30*, 1800561.

[2] a)Y. Q. Wu, W. X. Wang, J. Ming, M. L. Li, L. Q. Xie, X. M. He, J. Wang, S. Q. Liang, Y. P. Wu, *Adv. Funct. Mater.* **2019**, *29*, 1805978; b)E. R. Logan, J. R. Dahn, *Trends Chem.* **2020**, *2*, 354; c)X. D. Lin, G. D. Zhou, J. P. Liu, J. Yu, M. B. Effat, J. X. Wu, F. Ciucci, *Adv. Energy Mater.* **2020**, *10*, 2001235.

[3] a)Y. K. Sun, S. T. Myung, B. C. Park, J. Prakash, I. Belharouak, K. Amine, *Nat. Mater.* **2009**, *8*, 320; b)Y. K. Sun, Z. Chen, H. J. Noh, D. J. Lee, H. G. Jung, Y. Ren, S. Wang, C. S. Yoon, S. T. Myung, K. Amine, *Nat. Mater.* **2012**, *11*, 942; c)A. Manthiram, J. C. Knight, S.-T. Myung, S.-M. Oh, Y.-K. Sun, *Adv. Energy Mater.* **2016**, *6*, 1501010.

[4] a)J. Ma, P. Hu, G. Cui, L. Chen, *Chem. Mater.* **2016**, *28*, 3578; b)G. Xu, C. Pang, B. Chen, J. Ma, X. Wang, J. Chai, Q. Wang, W. An, X. Zhou, G. Cui, L. Chen, *Adv. Energy Mater.* **2018**, *8*, 1701398; c)Y. Ma, K. Chen, J. Ma, G. Xu, S. Dong, B. Chen, J. Li, Z. Chen, X. Zhou, G. Cui, *Energy Environ. Sci.* **2019**, *12*, 273.

[5] a)S. Ye, L. Wang, F. Liu, P. Shi, H. Wang, X. Wu, Y. Yu, *Adv. Energy Mater.* **2020**, *10*, 2002647; b)H. Zheng, H. Xiang, F. Jiang, Y. Liu, Y. Sun, X. Liang, Y. Feng, Y. Yu, *Adv. Energy Mater.* **2020**, *10*, 2001440; c)Q. Li, Z. Cao, G. Liu, H. Cheng, Y. Wu, H. Ming, G. T. Park, D. Yin, L. Wang, L. Cavallo, Y. K. Sun, J. Ming, *J. Phys. Chem. Lett.* **2021**, *12*, 4857.

[6] H. Xue, Y. Wu, Y. Zou, Y. Shen, G. Liu, Q. Li, D. Yin, L. Wang, J. Ming, *Adv. Funct. Mater.* **2020**, *30*, 1910657.

[7] a)L. Zhou, J. Zhang, Y. Q. Wu, W. X. Wang, H. Ming, Q. J. Sun, L. M. Wang, J. Ming, H. N. Alshareef, *Adv. Energy Mater.* **2019**, *9*, 1902194; b)L. Zhou, Z. Cao, W. Wahyudi, J. Zhang, J.-Y. Hwang, Y. Cheng, L. Wang, L. Cavallo, T. Anthopoulos, Y.-K. Sun, H. N. Alshareef, J. Ming, *ACS Energy Lett.* **2020**, *5*, 766.

[8] a)J. Ming, Z. Cao, W. Wahyudi, M. Li, P. Kumar, Y. Wu, J.-Y. Hwang, M. N. Hedhili, L. Cavallo, Y.-K. Sun, L.-J. Li, *ACS Energy Lett.* **2018**, *3*, 335; b)J. Ming, Z. Cao, Y. Wu, W. Wahyudi, W. Wang, X. Guo, L. Cavallo, J.-Y. Hwang, A. Shamim, L.-J. Li, Y.-K. Sun, H. N. Alshareef, *ACS Energy Lett.* **2019**, *4*, 2613; c)J. Ming, Z. Cao, Q. Li, W. Wahyudi, W. Wang, L. Cavallo, K.-J. Park, Y.-K. Sun, H. N. Alshareef, *ACS Energy Lett.* **2019**, *4*, 1584.

[9] a)S. Zhang, J. Ma, Z. Hu, G. Cui, L. Chen, *Chem. Mater.* **2019**, *31*, 6033; b)G. Xu, X. Shangguan, S. Dong, X. Zhou, G. Cui, *Angew. Chem. Int. Ed.* **2020**, *59*, 3400.

[10] Y. Zou, Y. Shen, Y. Wu, H. Xue, Y. Guo, G. Liu, L. Wang, J. Ming, *Chem.-Eur. J.* **2020**, *26*, 7930.

[11] Y. R. Zhang, Y. Katayama, R. Tatara, L. Giordano, Y. Yu, D. Fraggedakis, J. G. W. Sun, F. Maglia, R. Jung, M. Z. Bazant, Y. Shao-Horn, *Energ Environ Sci* **2020**, *13*, 183.

[12] A. T. S. Freiberg, M. K. Roos, J. Wandt, R. de Vivie-Riedle, H. A. Gasteiger, *J. Phys. Chem. A* **2018**, *122*, 8828.

[13] A. Tornheim, S. Sharifi-Asl, J. C. Garcia, J. Bareno, H. Iddir, R. Shahbazian-Yassar, Z. C. Zhang, *Nano Energy* **2019**, *55*, 216.

[14] a)J. Alvarado, M. A. Schroeder, M. H. Zhang, O. Borodin, E. Gobrogge, M. Olguin, M. S. Ding, M. Gobet, S. Greenbaum, Y. S. Meng, K. Xu, *Mater. Today* **2018**, *21*, 341; b)J. Fu, X. Ji, J. Chen, L. Chen, X. Fan, D. Mu, C. Wang, *Angew. Chem. Int. Ed.* **2020**, *59*, 22194; c)S. Liu, X. Ji, N. Piao, J. Chen, N. Eidson, J. Xu, P. Wang, L. Chen, J. Zhang, T. Deng, S. Hou, T. Jin, H. Wan, J. Li, J. Tu, C. Wang, *Angew. Chem. Int. Ed.* **2021**, *60*, 3661.

[15] S. Chen, J. Zheng, D. Mei, K. S. Han, M. H. Engelhard, W. Zhao, W. Xu, J. Liu, J. G. Zhang, *Adv. Mater.* **2018**, *30*, 1706102.

[16] M. N. He, C. C. Su, Z. X. Feng, L. Zeng, T. P. Wu, M. J. Bedzyk, P. Fenter, Y. Wang, Z. C. Zhang, *Adv. Energy Mater.* **2017**, *7*, 1700109.

[17] a)J. Xia, M. Nie, J. Burns, A. Xiao, W. Lamanna, J. Dahn, *J. Power Sources* **2016**, *307*, 340; b)J. Xia, K. J. Nelson, Z. H. Lu, J. R. Dahn, *J. Power Sources* **2016**, *329*, 387.

[18] a)Q. Q. Liu, D. J. Xiong, R. Petibon, C. Y. Du, J. R. Dahn, *J. Electrochem. Soc.* **2016**, *163*, A3010; b)Q. Q. Liu, R. Petibon, C. Y. Du, J. R. Dahn, *J. Electrochem. Soc.* **2017**, *164*, A1173.

[19] L. Ma, S. L. Glazier, R. Petibon, J. Xia, J. M. Peters, Q. Liu, J. Allen, R. N. C. Doig, J. R. Dahn, *J. Electrochem. Soc.* **2016**, *164*, A5008.

[20] E. R. Logan, D. S. Hall, M. M. E. Cormier, T. Taskovic, M. Bauer, I. Hamam, H. Hebecker, L. Molino, J. R. Dahn, *J. Phys. Chem. C* **2020**, *124*, 12269.

[21] E. R. Logan, E. M. Tonita, K. L. Gering, J. Li, X. W. Ma, L. Y. Beaulieu, J. R. Dahn, *J. Electrochem. Soc.* **2018**, *165*, A21.

[22] G. A. Elia, U. Ulissi, S. Jeong, S. Passerini, J. Hassoun, *Energy Environ. Sci.* **2016**, *9*, 3210.

[23] T. R. Tanim, M. G. Shirk, R. L. Bewley, E. J. Dufek, B. Y. Liaw, *J. Power Sources* **2018**, *381*, 56.

[24] G. Xu, S. Huang, Z. Cui, X. Du, X. Wang, D. Lu, X. Shangguan, J. Ma, P. Han, X. Zhou, G. Cui, *J. Power Sources* **2019**, *416*, 29.

[25] a)B. B. Lim, S. J. Yoon, K. J. Park, C. S. Yoon, S. J. Kim, J. J. Lee, Y. K. Sun, *Adv. Funct. Mater.* **2015**, *25*, 4673; b)G. Xu, L. Huang, C. Lu, X. Zhou, G. Cui, *Energy Storage Mater.* **2020**, *31*, 72.

[26] Y. Wu, M. Li, W. Wahyudi, G. Sheng, X. Miao, T. D. Anthopoulos, K.-W. Huang, Y. Li, Z. Lai, *ACS Omega* **2019**, *4*, 13972.

[27] S. Verdier, L. El Ouatani, R. Dedryvère, F. Bonhomme, P. Biensan, D. Gonbeau, *J. Electrochem. Soc.* **2007**, *154*, A1088.

[28] W. Zhao, J. Zheng, L. Zou, H. Jia, B. Liu, H. Wang, M. H. Engelhard, C. Wang, W. Xu, Y. Yang, J.-G. Zhang, *Adv. Energy Mater.* **2018**, *8*, 1800297.

[29] Y. Yu, P. Karayaylali, Y. Katayama, L. Giordano, M. Gauthier, F. Maglia, R. Jung, I. Lund, Y. Shao-Horn, *J. Phys. Chem. C* **2018**, *122*, 27368.

[30] Y. Q. Wu, H. Ming, M. L. Li, J. L. Zhang, W. Wahyudi, L. Q. Xie, X. M. He, J. Wang, Y. P. Wu, J. Ming, *ACS Energy Lett.* **2019**, *4*, 656.

[31] S. H. Song, M. Cho, I. Park, J. G. Yoo, K. T. Ko, J. Hong, J. Kim, S. K. Jung, M. Avdeev, S. Ji, S. Lee, J. Bang, H. Kim, *Adv. Energy Mater.* **2020**, *10*, 2000521.

[32] K. Kim, H. Ma, S. Park, N.-S. Choi, *ACS Energy Lett.* **2020**, *5*, 1537.

[33] X. H. Zhang, L. F. Zou, Y. B. Xu, X. Cao, M. H. Engelhard, B. E. Matthews, L. R. Zhong, H. P. Wu, H. Jia, X. D. Ren, P. Y. Gao, Z. H. Chen, Y. Qin, C. Kompella, B. W. Arey, J. Li, D. Y. Wang, C. M. Wang, J. G. Zhang, W. Xu, *Adv. Energy Mater.* **2020**, *10*, 2000368.

[34] X. Shangguan, G. Xu, Z. Cui, Q. Wang, X. Du, K. Chen, S. Huang, G. Jia, F. Li, X. Wang, D. Lu, S. Dong, G. Cui, *Small* **2019**, *15*, 1900269.

[35] Q. Zheng, Y. Yamada, R. Shang, S. Ko, Y.-Y. Lee, K. Kim, E. Nakamura, A. Yamada, *Nat. Energy* **2020**, *5*, 291.

[36] L. Zhang, H. Y. Wang, *J. Electrochem. Soc.* **2020**, *167*, 100506.

[37] A. V. Cresce, S. M. Russell, O. Borodin, J. A. Allen, M. A. Schroeder, M. Dai, J. Peng, M. P. Gobet, S. G. Greenbaum, R. E. Rogers, K. Xu, *Phys. Chem. Chem. Phys.* **2016**, *19*, 574.

[38] N. Chapman, O. Borodin, T. Yoon, C. C. Nguyen, B. L. Lucht, *J. Phys. Chem. C* **2017**, *121*, 2135.

[39] W. Zhang, Q. Wu, J. Huang, L. Fan, Z. Shen, Y. He, Q. Feng, G. Zhu, Y. Lu, *Adv. Mater.* **2020**, *32*, 2001740.

[40] a)W. Fan, N. W. Li, X. Zhang, S. Zhao, R. Cao, Y. Yin, Y. Xing, J. Wang, Y. G. Guo, C. Li, *Adv. Sci.* **2018**, *5*, 1800559; b)S. Wei, S. Inoue, D. Di Lecce, Z. Li, Y. Tominaga, J. Hassoun, *ChemElectroChem* **2020**, *7*, 2376; c)J. Popovic, G. Hasegawa, I. Moudrakovski, J. Maier, *J. Mater. Chem. A* **2016**, *4*, 7135.

[41] a)G. Liu, Z. Cao, L. Zhou, J. Zhang, Q. Sun, J. Y. Hwang, L. Cavallo, L. Wang, Y. K. Sun, J. Ming, *Adv. Funct. Mater.* **2020**, *30*, 2001934; b)J. Zhang, Z. Cao, L. Zhou, G. Liu, G.-T. Park, L. Cavallo, L. Wang, H. N. Alshareef, Y.-K. Sun, J. Ming, *ACS Energy Lett.* **2020**, *5*, 2651; c)L. Zhou, Z. Cao, J. Zhang, H. Cheng, G. Liu, G. T. Park, L. Cavallo, L. Wang, H. N. Alshareef, Y. K. Sun, J. Ming, *Adv. Mater.* **2021**, *33*, 2005993.

[42] Q. Li, Z. Cao, W. Wahyudi, G. Liu, G.-T. Park, L. Cavallo, T. D. Anthopoulos, L. Wang, Y.-K. Sun, H. N. Alshareef, J. Ming, *ACS Energy Lett.* **2020**, *6*, 69.

[43] a)L. Xing, O. Borodin, *Phys. Chem. Chem. Phys.* **2012**, *14*, 12838; b)O. Borodin, M. Olguin, C. E. Spear, K. W. Leiter, J. Knap, *Nanotechnology* **2015**, *26*, 354003; c)C. D. Malliakas, K. Leung, K. Z. Pupek, I. A. Shkrob, D. P. Abraham, *Phys. Chem. Chem. Phys.* **2016**, *18*, 10846; d)Y. Zheng, P. B. Balbuena, *J. Chem. Phys.* **2021**, *154*, 104702.

[44] a)K. Xu, *Chem. Rev.* **2004**, *104*, 4303; b)K. Xu, *Chem. Rev.* **2014**, *114*, 11503; c)N. Piao, S. Liu, B. Zhang, X. Ji, X. Fan, L. Wang, P.-F. Wang, T. Jin, S.-C. Liou, H. Yang, J. Jiang, K. Xu, M. A. Schroeder, X. He, C. Wang, *ACS Energy Lett.* **2021**, *6*, 1839; d)S. Liu, X. Ji, N. Piao, J. Chen, N. Eidson, J. Xu, P. Wang, L. Chen, J. Zhang, T. Deng, S. Hou, T. Jin, H. Wan, J. Li, J. Tu, C. Wang, *Angew. Chem. Int. Ed.* **2021**, *60*, 3661.

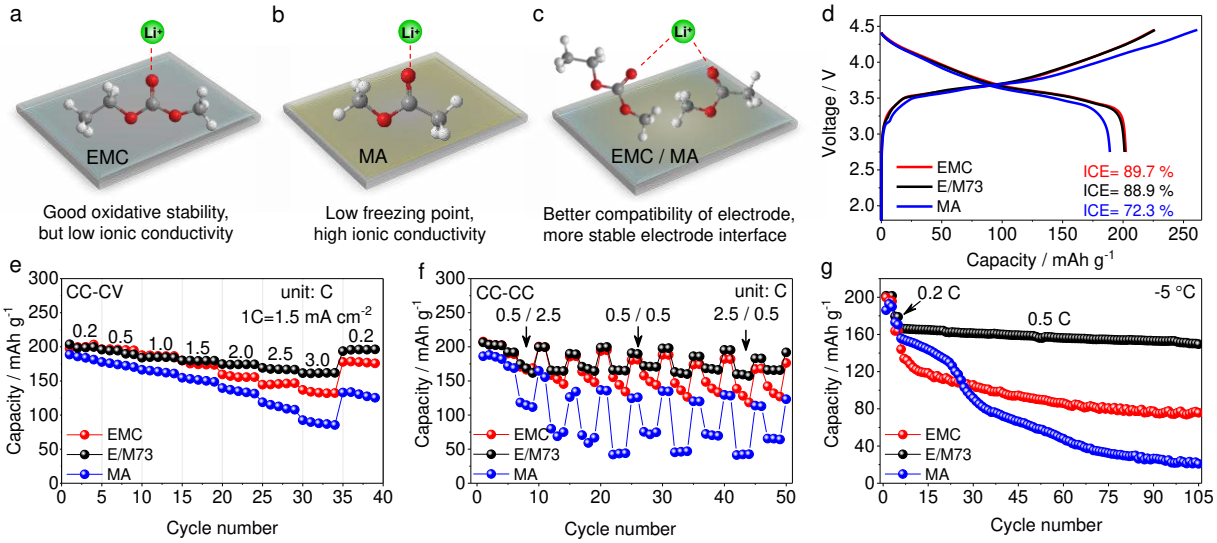

Figure 1. Characteristic of solvents and battery performance in different electrolytes. (a) Linear carbonate (EMC), (b) linear carboxylate (MA) and (c) binary solvent-based (EMC/MA) electrolytes. Comparative electrochemical performance of different electrolytes in the graphite || NCM622 cell at the high voltage of 4.45 V. (d) voltage vs. capacity profile and initial Coulombic efficiency (ICE) in the 1st cycle, (e) rate performance, (f) special fast charging/ discharging feature, and (g) long-term cycling at -5 °C under 0.5 C (C=1.5 mA cm^{-2}).

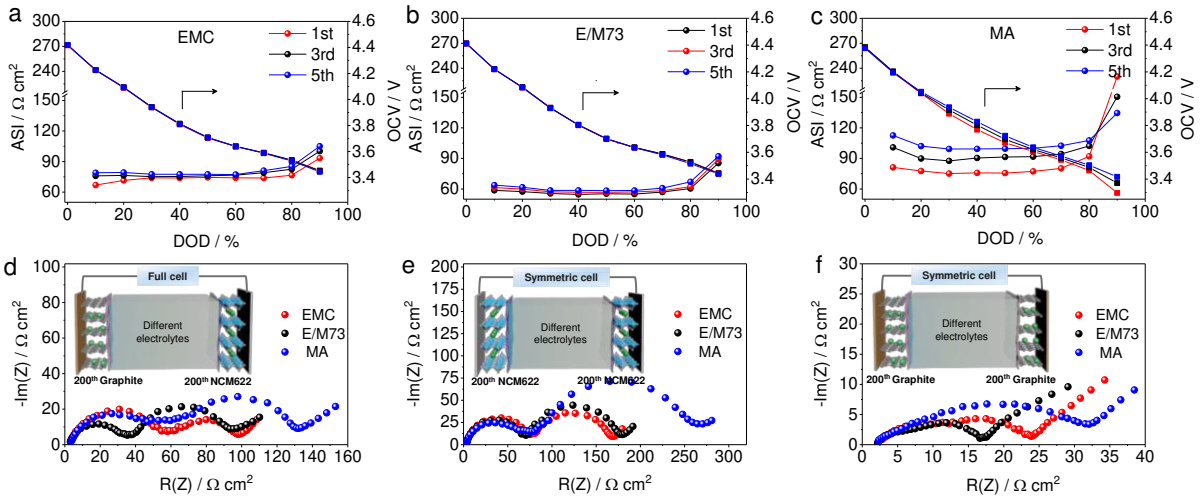

Figure 2. Comparison of power feature and interfacial impedance. Comparative ASI impedance and OCVs of the graphite || NCM622 cell by the HPPC used (a) EMC, (b) E/M73, and (c) MA electrolytes. EIS impedance of (d) graphite || NCM622 full cell and the symmetrical cell of (e) NCM622 || NCM622 and (f) graphite || graphite in different electrolytes after 200 cycles at 1C.

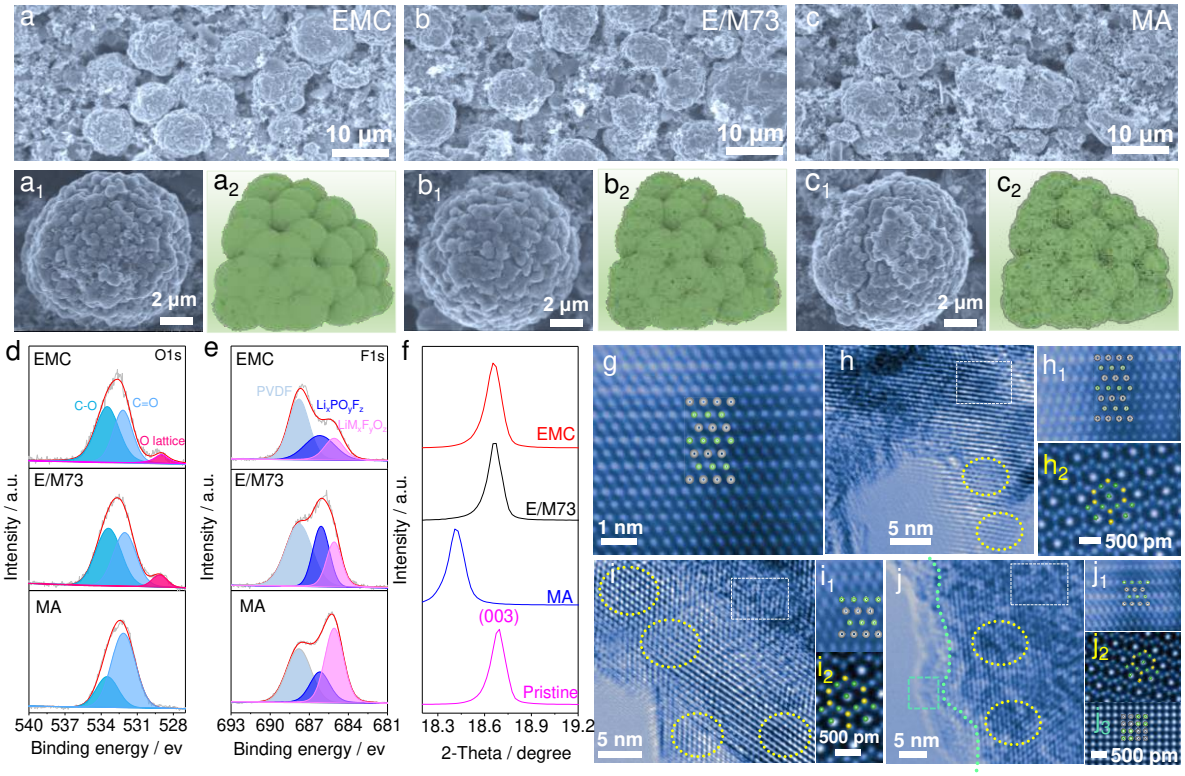

Figure 3. Characterizations of NCM622 cathode in the graphite || NCM622 cell employing different electrolytes after 200 cycles. SEM images and illustration of the cycled NCM622 particles from (a, a_1, a_2) EMC, (b, b_1, b_2) E/M73, and (c, c_1, c_2) MA electrolytes. XPS spectra of (d) O 1s and (e) F 1s of the cycled NCM622 electrode. XRD patterns of (f) (003) peak and HRTEM images of NCM622 surface layer from (g) pristine, (h, h_1, h_2) EMC, (i, i_1, i_2) E/M73, and (j, j_1, j_2, j_3) MA electrolytes.

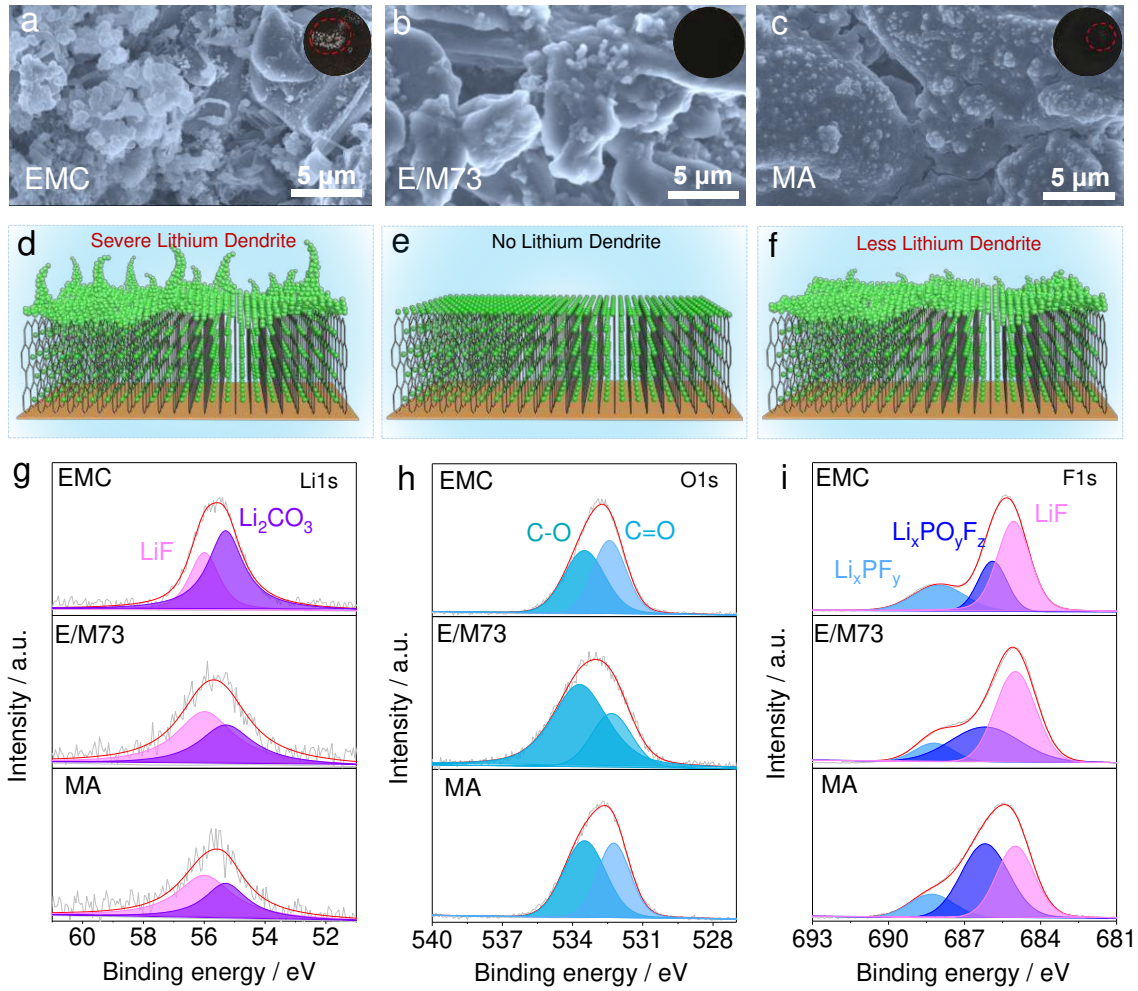

Figure 4. Characterizations of graphite anode in the graphite || NCM622 cell employing different electrolytes after 200 cycles. SEM images and illustration of the deposition of lithium metal on cycled graphite electrode in (a, d) EMC, (b, e) E/M73, and (c, f) MA electrolytes. XPS spectra of (g) Li 1s, (h) O 1s, and (i) F 1s of cycled graphite electrode.

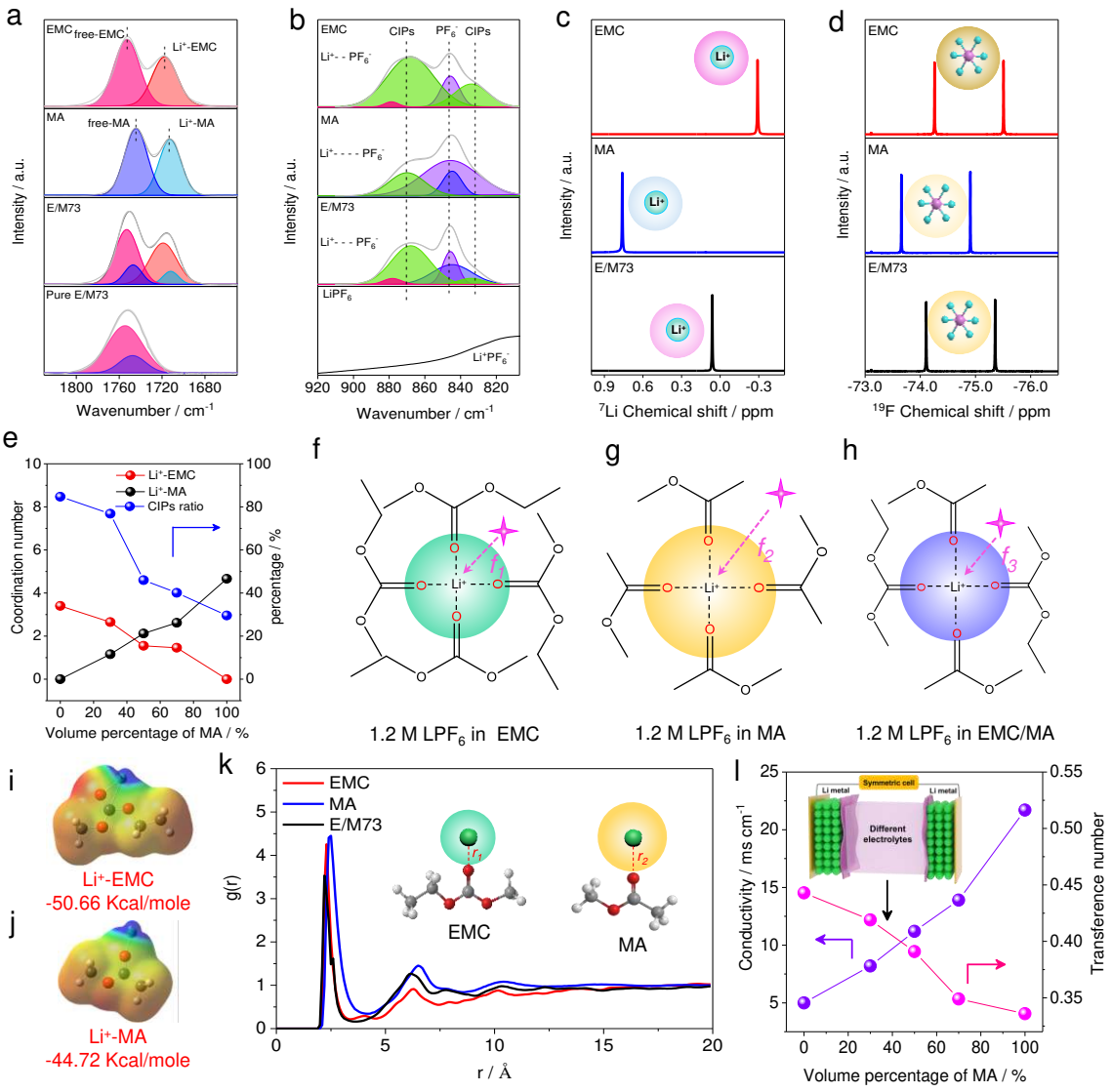

Figure 5. Electrolyte analysis and solvation behaviors in different electrolytes. FTIR spectra of (a) Li^+-solvent, (b) free-PF_6^- or CIPs, (c) ^{7}Li-NMR spectra of Li^+, and (d) ^{19}F-NMR spectra of PF_6^- in different electrolytes. (e) Coordination number of Li^+-solvent and CIPs ratio obtained from the FTIR fitting results. Frequency of PF_6^- contact with the Li^+ in the (f) EMC, (g) MA, and (h) E/M73 electrolytes. Binding energy of (i) Li^+-EMC and (j) Li^+-MA. (k) Radial distribution function (RDF) of Li^+-O and (l) conductivity and transference number of Li^+ ions in different electrolytes.

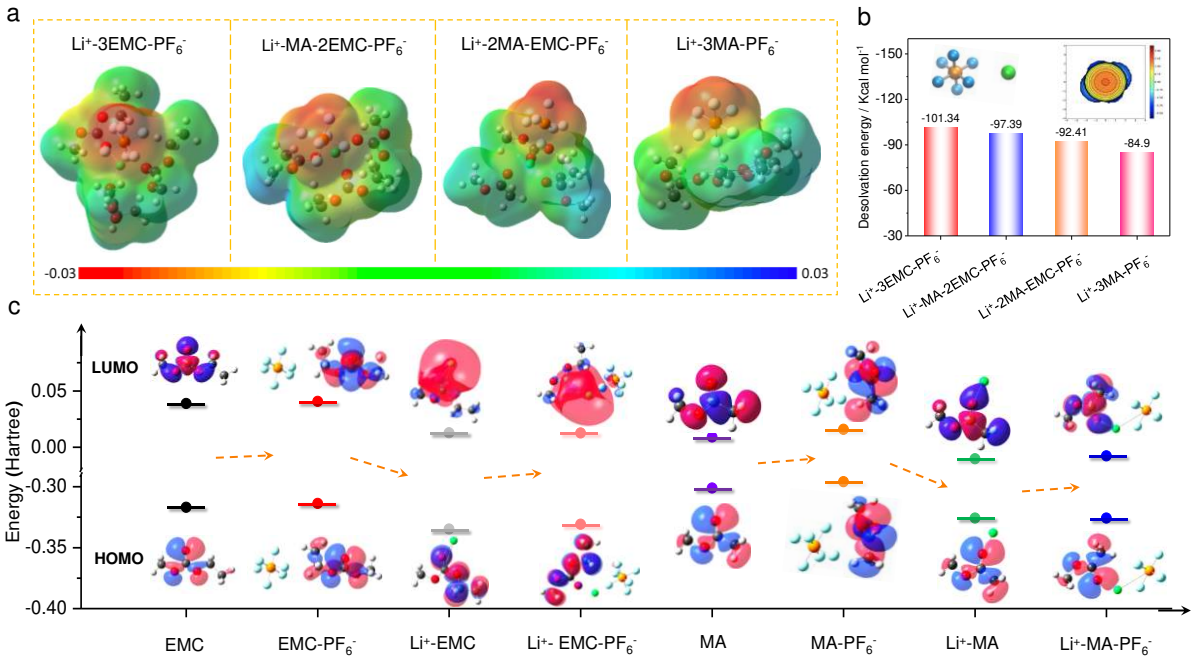

Figure 6. Simulated solvation behaviors in different solvents. (a) Electrostatic potential mapping about electron distribution for different Li^+-solvent-PF_6^- pair. (b) Desolvation energies between Li^+-solvents-PF_6^- obtained by DFT calculations (Right inset is the simulation snapshot of Buried volume (%VBur) calculations for PF_6^-). (c) LUMO and HOMO energy of the solvent, solvent-PF_6^-, Li^+-solvent, and Li^+-solvent-PF_6^- pair (Insets are molecular orbital simulation snapshots of LUMO and HOMO).

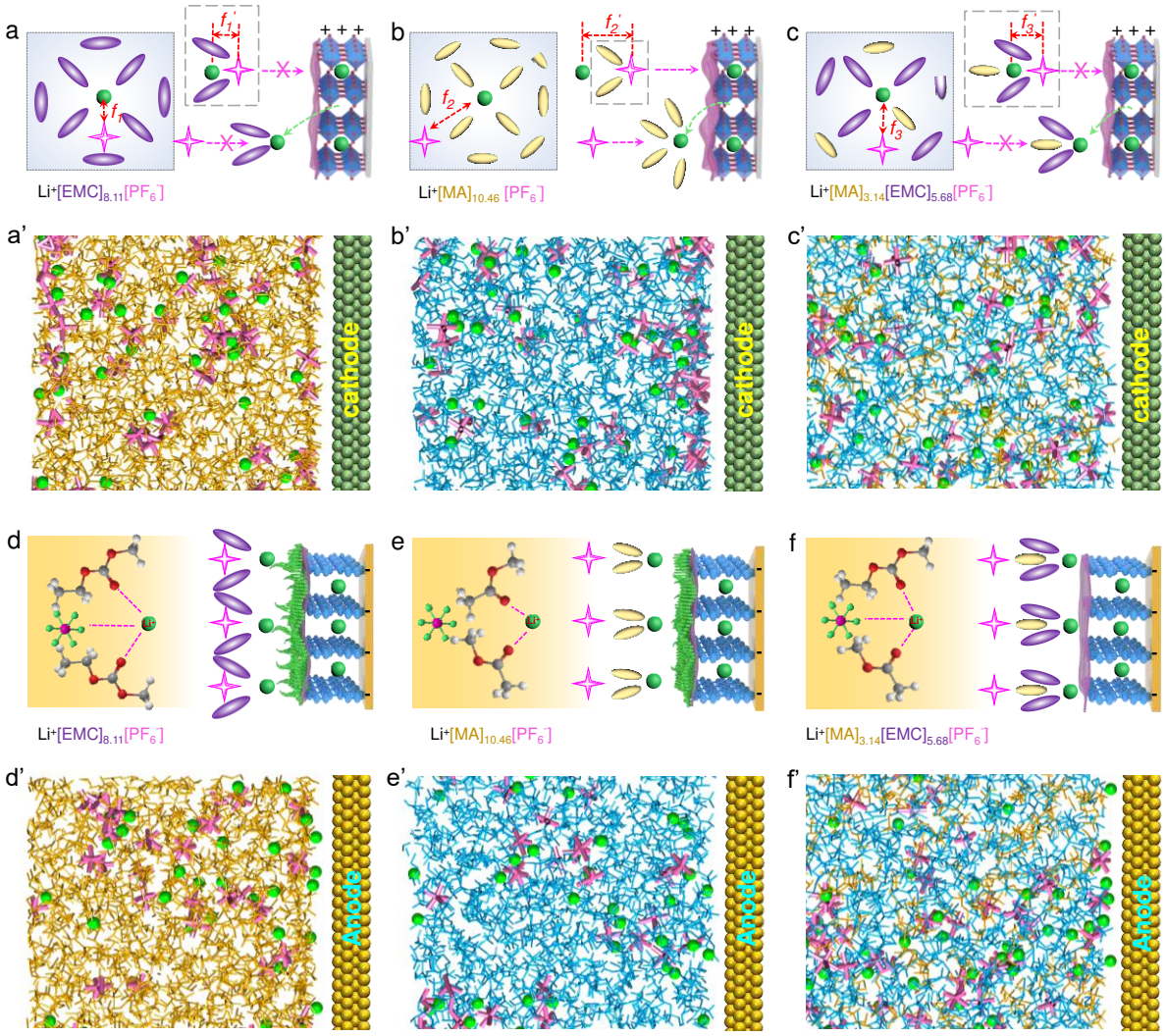

Figure 7. Interfacial behavior and simulation from the bulk electrolyte to electrode interphase. (a-c) Cathode interfacial model and (a'-c') simulated electrolyte behavior on the cathode/electrolyte interphase, (d-f) anode interfacial model and (d'-f') simulated electrolyte behavior on the anode/electrolyte interphase in the EMC, MA, and E/M73 electrolytes, respectively.

The table of contents entry:

A new additive-free high voltage electrolyte that affords high stability **at high voltage (4.5 V *vs.* Li/Li$^+$)**, **lithium-dendrite free** upon **fast-charging** operations, and superior **long-term battery performances at low-temperature** is designed. More importantly, **a new solvation structure-related interfacial model**, involving the molecular-scale interactions between the lithium-ion, anion, and solvents on the electrolyte-electrode surface, is presented to interpret the high performance. **This is a pioneering study** to explore the **dynamic mutual-interaction interfacial behaviors** on the lithium layered oxide cathode and graphite anode simultaneously in a battery. This model can explain the electrode performance from a molecular interaction that d**iffers from the solid electrolyte interphase** and then **set a new guideline** to design versatile electrolytes for metal-ion batteries.

Yeguo Zou,† Zhen Cao,† Junli Zhang, Wandi Wahyudi, Yingqiang Wu, Gang Liu, Qian Li, Haoran Cheng, Dongyu Zhang, Geon-Tae Park, Luigi Cavallo, Thomas D. Anthopoulos, Limin Wang, Yang-Kook Sun,* Jun Ming**

Interfacial Model Deciphering High-Voltage Electrolytes for High Energy Density, High Safety, and Fast-Charging Lithium-Ion Batteries

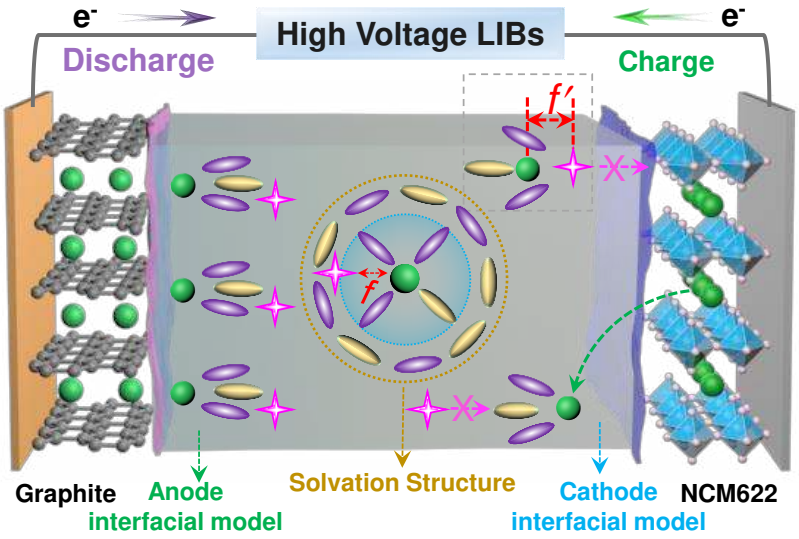

Supporting Information

Interfacial Model Deciphering High-Voltage Electrolytes for High Energy Density, High Safety, and Fast-Charging Lithium-Ion Batteries

Yeguo Zou,† Zhen Cao,† Junli Zhang, Wandi Wahyudi, Yingqiang Wu, Gang Liu, Qian Li, Haoran Cheng, Dongyu Zhang, Geon-Tae Park, Luigi Cavallo, Thomas D. Anthopoulos, Limin Wang, Yang-Kook Sun,* Jun Ming**

Y. Zou, Dr. Y. Wu, G. Liu, H. Cheng, Dr. Q. Li, D. Zhang, Prof. L. Wang, Prof. J. Ming
State Key Laboratory of Rare Earth Resource Utilization, Changchun Institute of Applied Chemistry, CAS, Changchun 130022, China
E-mail: jun.ming@ciac.ac.cn

Y. Zou, G. Liu, H. Cheng, D. Zhang, Prof. L. Wang, Prof. J. Ming
University of Science and Technology of China
Hefei 230026, China

Dr. Z. Cao, Dr. W. Wahyudi, Prof. L. Cavallo, Prof. T. Anthopoulos
Physical Science and Engineering Division (PSE), King Abdullah University of Science and Technology (KAUST), Thuwal, 23955-6900, Saudi Arabia

Prof. J. Zhang
Key Laboratory of Magnetism and Magnetic Materials of the Ministry of Education, School of Physical Science and Technology, Lanzhou University, Lanzhou 730000, China
E-mail: zhangjl@lzu.edu.cn

G. T. Park, Prof. Y. K. Sun
Department of Energy Engineering, Hanyang University
Seoul 133-791, Republic of Korea
E-mail: yksun@hanyang.ac.kr

†These authors contributed equally

Keywords: Lithium-ion batteries, high-voltage electrolytes, solvation structure, electrolyte/electrode interface, fast charging

Experimental Section

Electrolyte and electrode preparation. The chemicals of ethyl methyl carbonate (EMC), methyl acetate (MA), and lithium hexafluorophosphate ($LiPF_6$) were purchased from Huzhou Kunlun Power Battery Materials Co., Ltd. The electrolyte was prepared as below. Typically, 1.2 M $LiPF_6$ was dissolved in the EMC/MA mixture, in which the solvent ratio was controlled at 10:0, 7:3, 5:5, 3:7, and 0:10 (v/v), respectively. The abbreviation of the electrolytes is denoted as EMC, E/M73, E/M55, E/M37, and MA respectively according to the solvent ratio. The $LiNi_{0.6}Co_{0.2}Mn_{0.2}O_2$ (NCM622) and graphite powders were purchased from Guangdong Canrd New Energy and Shanghai Shanshan Tech Co., Ltd, China, respectively. The cathode was prepared by mixing NCM622, Super C45, KS-6, and polyvinylidene fluoride binder with a mass ratio of 92.5:3:1.5:3 in N-methyl-2pyrrolidone. The anode was prepared by mixing graphite, Super C45, carboxymethyl cellulose (CMC), and styrene-butadiene rubber (SBR) binder with a mass ratio of 94.5:1.5:1.5:2.5 in water. The mixtures were milled by using a Hasai planetary mixer for 5 min. Then, the uniform slurry was coated on the Al and Cu foils, respectively. Finally, the NCM and graphite electrodes were dried at 120 °C and 80°C in a vacuum for 10 h before using them, respectively. The mass loadings of the cathode and anode were about 7.5 mg cm^{-2} and 5.5 mg cm^{-2}, respectively. Also, a higher mass loading of the cathode (9.5 mg cm^{-2}) and anode (6.9 mg cm^{-2}) was evaluated in the full cell to prove the practical application capability of as-designed electrolyte.

Electrochemical performance Test. All the batteries were assembled using the 2025-type coin cell with polypropylene (PP) separator (Celgard 2400) and disassembled in an argon-filled glovebox (the content of O_2 and H_2O was maintained below 3.0 ppm). The assembled full cell (i.e., graphite || NCM622) were charged to 4.45 V (4.5 V vs. Li/Li^+) and then discharged to 2.75

V at 0.1C (1 C = 1.5 mA cm^{-2}) in the first cycle. Then the Constant current-constant voltage (CC-CV) protocol was applied in the normal cycling and rate test. Firstly, it was constant-current charged at 0.2 C (CC) to the 4.45 V, and then the cell was constant-voltage charged until the current density to 0.1 C (CV) and discharged to 2.75 V at 0.2 C. After the above activation process (i.e., 3 cycles at 0.2 C), the cell was cycled at 1C for long cycling or performed power capacity at the different rates (i.e., 0.5 C-3.0 C), in which the constant-voltage charging current was set at 0.2 C. In other special rate tests, the cells were charged at 0.5C and discharged at 2.5 C or were charged 2.5 C and discharged 0.5 C without the constant voltage process. The Li || Li symmetrical cells were comprised of two Li metal pieces (13.6 mm in diameter). Long-term galvanostatic cycling was performed at 0.5 mA cm^{-2} with a certain cut-off capacity of 1 mAh cm^{-2}. In the low-temperature cycling test, the full cell was performed under 0.2 C at 25 °C for two cycles first, then the cell was cycled under 0.5C at -5 °C. All the (dis-)charge curves were recorded by the Neware instrument.

Electrochemical impedance test. The hybrid pulse power characterization (HPPC) (i.e., DC impedance test) was tested by the following protocol, firstly the cell was fully charged and then discharged at a 0.1 C rate after two cycles, then the discharge procedure was repeated from 10 to 90% depth of discharge (DOD), each followed by a 1 h rest period before applying the next sequence. The pulse profiles were measured at every 10% DOD, in which a 10 s 3.0 C discharge pulse and a 2.25 C regenerative charge pulse current were applied to the cells. There were 40 s rest periods between discharge and regenerative pulses (**Figure S5**). The SP-PVDF/Al electrode (i.e., Super C45 : PVDF = 9 : 1 by weight) was used as the working electrode in the linear sweep voltammetry (LSV) test and stepwise potential sweep measurement, in which the Li metal was used as the counter and reference electrode. In the LSV test, the voltage window

was set from 3.0 to 6.0 V using a scan rate of 1 mV s^{-1}. In the stepwise potential sweep test, the current vs. time plots were obtained by applying increasing voltage steps of 0.1 V. All the curves were acquired by the electrochemical station *Bio-Logic VMP3*.

The electrochemical impedance spectroscopy (EIS) measurements (i.e., AC impedance test) were tested using the *Bio-Logic VMP3* between a frequency range of 300 kHz and 10 mHz and a sinusoidal amplitude of 10 mV. All the full cells were tested under the stage of 50% DOD (i.e., depth of discharge) and at 25 °C. The electrodes of symmetrical batteries (NCM622 || NCM622 and graphite || graphite) were obtained from the full cells that were also discharged to 50% DOD after the desired cycling. After disassembling in the glovebox, the symmetrical cells were assembled using the cycled electrodes.

Characterizations. The XRD data were obtained by the powder X-ray diffractometer (XRD, Bruker D8 ADVANCE) with Cu Kα radiation (λ = 1.5406 Å) in the 2θ range of 10° to 80° at a scan speed of 1° min^{-1} for graphite and NCM power, respectively. The morphology of the pristine and cycled electrode materials was examined by scanning electron microscopy (SEM, Hitachi S-4800) and transmission electron microscopy (TEM, Thermo Fisher Talos 200S), while their atom-resolved images were obtained with a probe-corrected scanning transmission electron microscope (STEM, FEI Titan 80-200). The XPS spectra of the graphite and NCM electrodes were measured by X-ray photoelectron spectroscopy (XPS, ESCALABMKLL) with Al Kα radiation, which emits 1.4866 keV X-ray with the corresponding wavelength of 8.53 Å. All the cycled electrodes were rinsed with pure anhydrous EMC solvent to remove residual $LiPF_6$, dried, and then sealed in the glovebox before being transferred for characterizations. In the Differential Scanning Calorimetry (DSC) experiments, the de-lithiated cathode (NCM622) electrodes were retrieved from the coin cell that charged to 4.5 V (vs. Li/Li^+) and rinsed

thoroughly with dimethyl carbonate (DMC) solvent. The dried cathode materials were scratched off from the current collector, then mixed with different electrolytes in the weight ratio of 10:1 in an Ar-filled glovebox. Then, 7 mg as-prepared samples (i.e., a mixture of the de-lithiated NCM622 cathode and electrolytes) were sealed in a 30 μL high-pressure stainless-steel DSC vessel with a gold-plated copper. The measurements were conducted on a Pyris 1 differential scanning calorimeter (NETZSCH, DSC 200 PC). The DSC profiles were recorded between 50 and 350 °C with a scan rate of 5°C min^{-1}.

The contact angles of electrolytes were measured by a contact angle meter (Kruss DSA 10). Electrolyte conductivities were performed on a conductivity meter (Five Easy Plus^{TM}-FE38, Mettler Toledo Co., Ltd) at 25°C. The calculation of t_{Li^+} resulted from the Bruce-Vincent-Evans equation in **Figure S10**f. The ΔV is the applied polarization voltage. The I_0 and R_0 are the initial currents and interfacial resistance before polarization, respectively, while the I_{ss} and R_{ss} are the steady-state currents and interfacial resistance after polarization, respectively. The chronoamperometry was carried out by symmetrical Li || Li cells with applying a 10 mV (ΔV) direct current (DC) pulse for 10 min, while the EIS measurement was performed by using an alternating current (AC) signal with an amplitude of 10 mV within the 100 kHz-1 Hz frequency range. The calculation of t_{Li^+} resulted from the Bruce-Vincent-Evans equation in **Figure S10**f. The ΔV is the applied polarization voltage (ΔV = 10 mV), the I_0, and R_0 are the initial currents and interfacial resistance before polarization, respectively, while the I_{ss} and R_{ss} are the steady-state currents and interfacial resistance after polarization for 600 s, respectively. Fourier-transform infrared (FTIR) was collected by the VERTEX 70 FTIR spectrometer, where the lithium salt or the electrolyte was placed directly on the windows testing holders with 2 cm^{-1} resolutions with 32 total scans. All FTIR spectra were processed and analyzed by OMNIC and

Originlab software. Finally, the Nuclear magnetic resonance (NMR) analysis of the electrolyte was carried out on Bruker AV-Ⅲ 600 MHz Liquid NMR.

Theoretical simulation. The binding energy and molecular orbitals were studied based on the gas phase calculations and the implicit solvent models using the Gaussian09 package.[3] Firstly, the structural optimizations were performed using the PBE0 level of density functional theory,[4] together with the DEF2TZVP basis sets.[5] The vdW interactions were described using Grimme's dispersion correction.[6] Thereafter, the structural were further optimized using the SMD implicit solvent model[7] with the dielectric constant of 5. The bulk properties of the systems were evaluated using the AMBER force field [8] and the missing parameters were obtained using the AMBER-GAFF method.[9] The systems were firstly equilibrated within the NPT ensemble [10] with the 1 bar pressure and 300 K temperature for 5 ns. Then, the last frame of the system was quenched from 3000K to 300K in the NVT ensemble[8a] for a sum of 30 ns. Next, the system was re-equilibrated within the NPT ensemble with 1bar pressure and 300 K temperature. The above process was repeated 4 times, and the volume is converged to a fixed value. Thereafter, the system was simulated in the NVT ensemble for 50 ns, and the last 30ns were used to calculate the radial distribution functions. At the interface, the systems were further simulated for 100 ns.

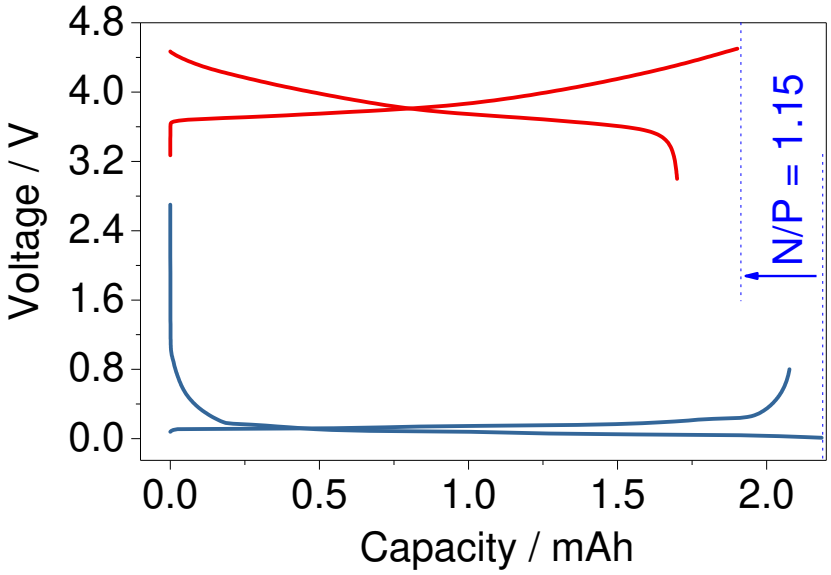

Figure S1. Capacity match of the cathode and anode in C || NCM622 full cell, where the N/P ratio is 1.15.

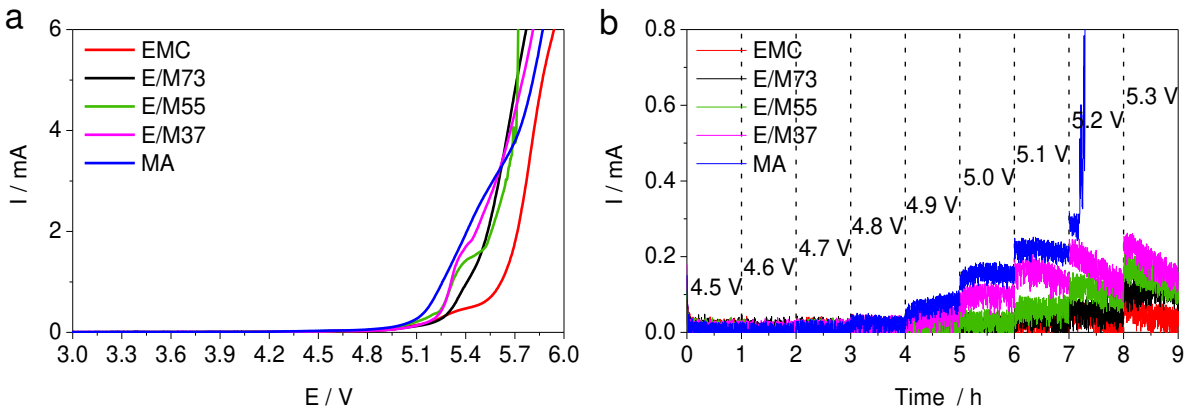

Figure S2. Oxidative stability of the various electrolytes. (a) Linear sweep voltammograms (LSV) profiles of SP-PVDF/Al electrodes || Li with the scan rate of 1 mV s^{-1} from 3.0 V to 6 V. (b) Current vs. time profile of the SP-PVDF/Al electrodes || Li applied to a stepwise potential sweep (potential increasing by 0.1 V each 1 h).

The oxidative current of the electrolyte increases gradually as increasing the volume ratio of MA in the electrolyte, while the electrolyte can still be stabilized at the high voltage of 4.8 V vs. Li/Li^+, as shown in the LSV test (**Figure S2**a). Thus, the cell can work well at 4.5 V vs. Li/Li^+. This result is further confirmed by the harsher stepwise potential sweep test, where the oxidative current has a trend to be increased when the voltage is higher than 4.8 V vs. Li/Li^+ (**Figure S2**b). But, the oxidative current increment of E/M73 and EMC electrolytes is relatively small. All these results prove that the E/M73 electrolyte is stable under the high potential (e.g., 4.5 V vs. Li/Li^+).

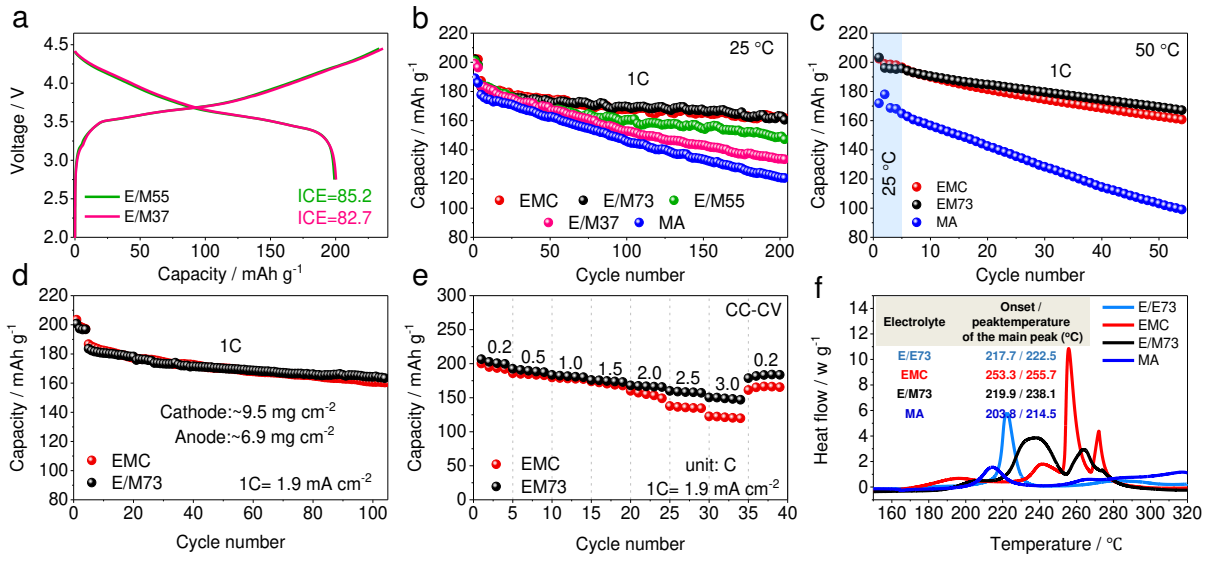

Figure S3. Comparative electrochemical performance of the high-voltage graphite || NCM622 cell employing different electrolytes. (a) Initial Coulombic efficiency (ICE) of the full cell used E/M55 and E/M37 electrolyte and cycling performance of the full cell under 1C (C=1.5 mA cm^{-2}) at (b) 25°C and (c) 50°C. (d) Cycling stability and (e) power capacity of the full cell with higher mass loading electrode (i.e., cathode, ~9.5 mg cm^{-2}; anode, ~6.9 mg cm^{-2}). (f) Differential scanning calorimetry traces showing heat flow from the reaction of the different electrolytes with de-lithiated NCM622 (i.e., charged to 4.5V vs. Li/Li^{+}).

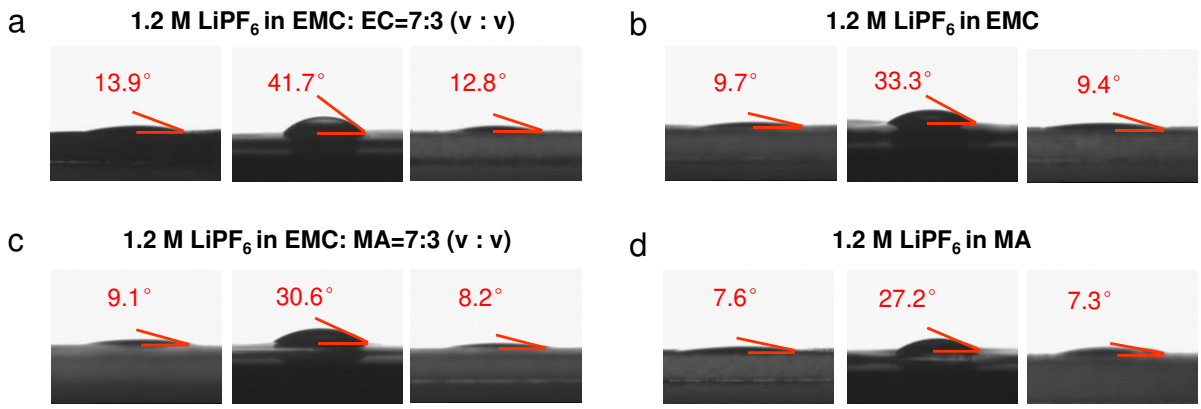

Figure S4. Contact angles of different electrolytes on the NCM622 cathode, PP separator, and graphite anode, respectively.

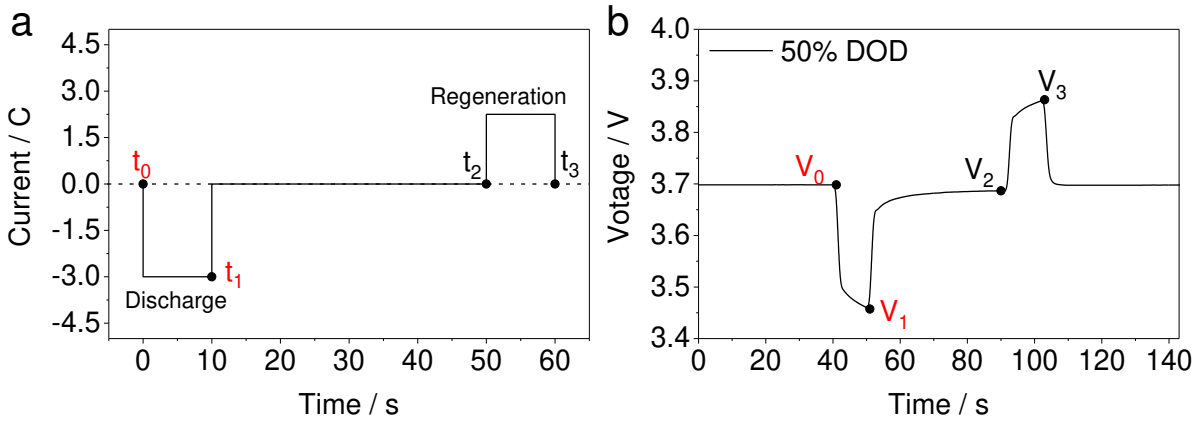

Figure S5. One pulse protocol of the HPPC test for graphite || NCM622. (a) Current curve and (b) voltage curve as a function of time (e.g., 50 % DOD).

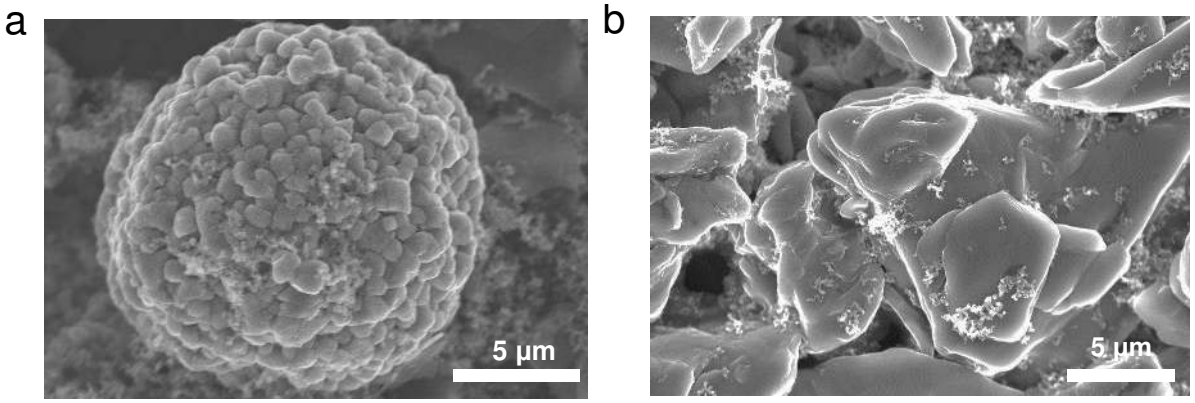

Figure S6. SEM images of (a) the secondary particles of pristine NCM622 and (b) the surface of pristine graphite.

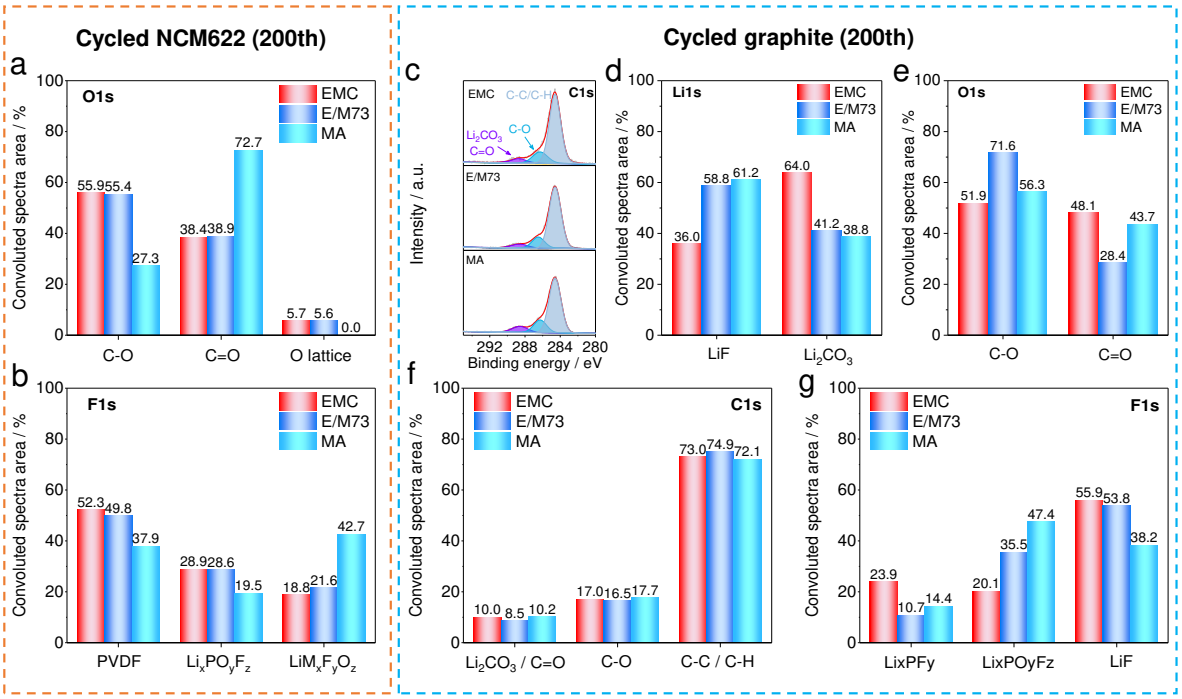

Figure S7. Component analysis of electrolyte decomposition by XPS spectra. Convoluted spectra area percentage of cycled NCM622 electrode, including (a) O1s and (b) F1s. (c) C1s spectra of cycled graphite. Convoluted spectra area percentage of cycled graphite, including (d) Li1s, (e) O1s, (f) C1s, and (g) F1s.

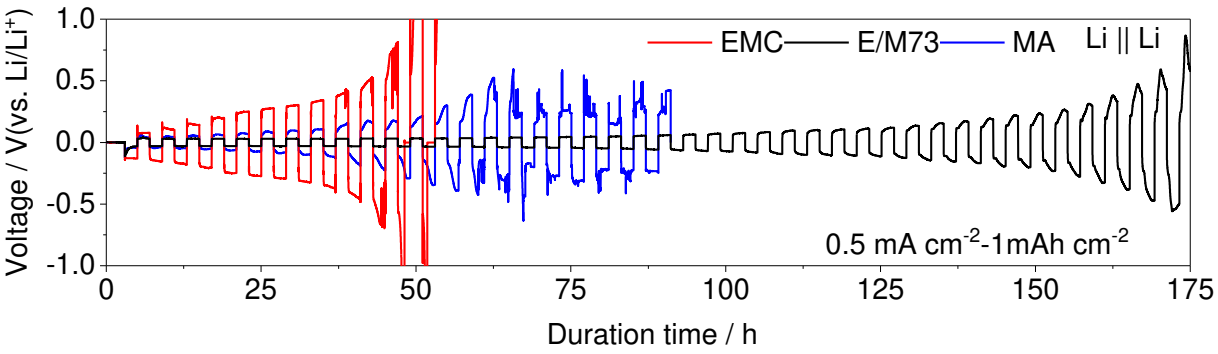

Figure S8. Cycling performance of Li || Li symmetric cell with EMC, E/M73, and MA electrolytes under the current density of 0.5 mA cm^{-2} with the capacity of 1 mAh cm^{-2} conditions.

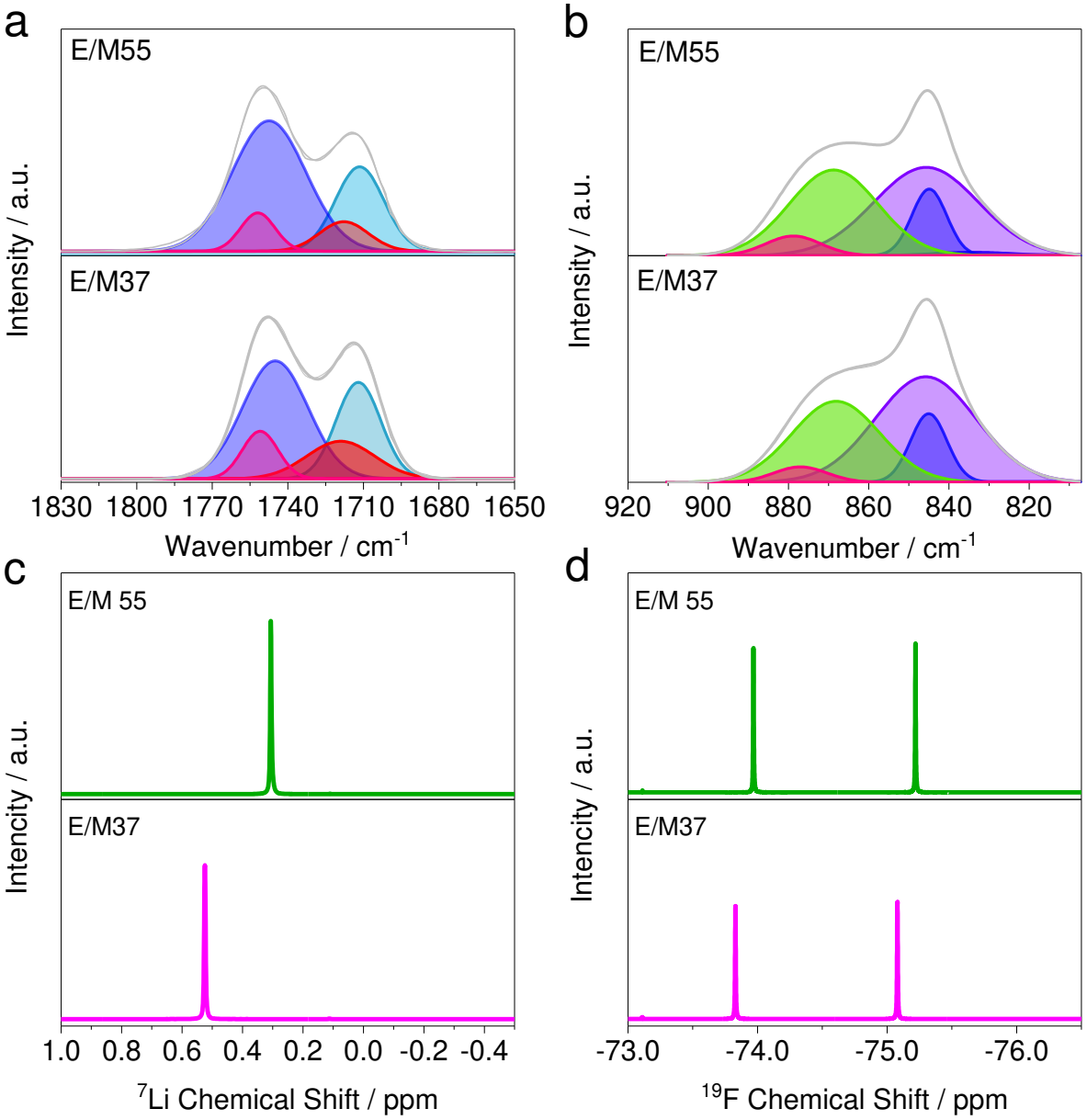

Figure S9. Fitting FTIR spectra of E/M55 and E/M37 electrolytes in (a) Li^+-solvent (1830 cm^{-1}~1650 cm^{-1}) and (b) free-PF_6^- or CIPs in different solvents (920 cm^{-1}~805 cm^{-1}), and (c) ^{7}Li-NMR spectra and (d) ^{19}F-NMR spectra of $LiPF_6$ in different kinds of solvents.

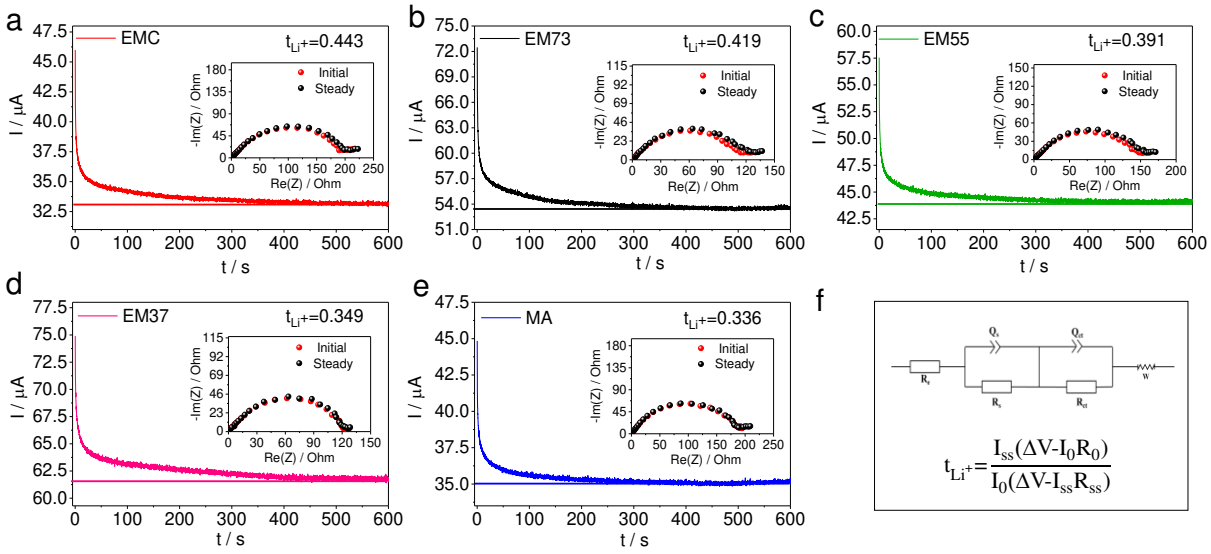

1 **Figure S10.** Current variation with the polarization of a Li || Li symmetric cell with an applied
2 potential of 10 mV and EIS test before and after polarization. (a) EMC, (b) E/M73, (c) E/M55,
3 (d) E/M37, (e) MA electrolytes, and (f) equivalent circuit model and the calculated formula of
4 Li^+ transference number.

Table S1. Comparison of the electrochemical performance of the high-voltage LIBs employing E/M73 electrolytes and those using different electrolytes reported before.

Battery	Electrolyte	Voltage (V)	Initial discharge capacity (mAh g^{-1})	Cycling and rate performance	Ref.
Graphite ‖ NCM333	1.0 M LiDFOB in ADN/DMC+2 wt.%FEC	3.0~4.5 (vs. Li/Li^+)	189.4	86% after 40 cycles at 0.5 C; no rate	[9]
Graphite ‖ NCM333	1.15 M $LiPF_6$ in EC/EMC+0.1wt.% dopamine	3.0~4.5	~165.0	90.1% after 100 cycles at 1.0 C; **117 mAh g^{-1} (3C)**	[10]
Graphite ‖ NCM333	1.0 M $LiPF_6$ in EC/DMC/EMC +0.2 wt.% TFPM	3.0~4.6	191.6	75.4 % after 100 cycles at 0.2 C; no rate	[11]
Graphite ‖ NCM424	1.0 M $LiPF_6$ in EC/DMC/EMC+1 wt.% TMSP	2.75~4.35	176.6	90.8 % after 70 cycles at 1.0 C; **112.9 mAh g^{-1} (3C)**	[12]
Graphite ‖ NCM523	1.0 M $LiPF_6$ in EC/DMC/PC+2 wt.% PS	2.7~4.5 (vs. Li/Li^+)	~195.0	88.0 % after 120 cycles at 1.0 C; no rate	[13]
Graphite ‖ NCM523	1.0 M $LiPF_6$ in EC/EMC+ 1wt.%TFEOP	3.0~4.6	193.5	83.6% after 100 cycles at C/3; no rate	[14]
Graphite ‖ NCM622	1.0 M $LiPF_6$ in EC/ EMC+1 wt.% CEP	3.0~4.5	~200.0	81.5 % after 50 cycles at 1.0 C; **150 mAh g^{-1} (3C)**	[15]
Graphite ‖ NCM622	1.2 M $LiPF_6$ DFEC/TFPMS	3.0~4.5	195.9	81.8% after 400 cycles at 0.5 C; no rate	[16]
Graphite ‖ NCM622	1.2 M $LiPF_6$ in EMC/MA	2.75~4.45	201.2	87.4% after 200 cycles at 1C; **162 mAh g^{-1} (3C)**	This Work

Table S2. EIS impedance of the full cell using different electrolytes after 200 cycles at 1 C.

Electrolytes	Graphite || NCM622 R(Z) / Ω cm^2	NCM622 || NCM622 R(Z) / Ω cm^2	Graphite || Graphite R(Z) / Ω cm^2
EMC	94.7	166.6	21.1
E/M73	92.2	176.8	14.4
MA	128.6	267.3	29.8

Table S3. The coordination number of Li^+-solvent, total coordination number, and CIPs ratio of 1.2 M $LiPF_6$ in EMC, E/M73, E/M55, E/M37, and MA were calculated by the fitting result of FTIR.

Electrolytes	Coordination number			CIP ratio
	EMC	MA	Total	
EMC	3.40	0	3.40	84.7 %
E/M73	2.65	1.16	3.81	76.8 %
E/M55	1.55	2.12	3.67	46.0 %
E/M37	1.46	2.62	4.08	40.1 %
MA	0	4.66	4.66	29.6 %

References

[1] Gaussian 09, Revision d.02, M. J. Frisch, G. W. Trucks, H. B. Schlegel, G. E. Scuseria, M. A. Robb, J. R. Cheeseman, G. Scalmani, V. Barone, G. A. Petersson, H. Nakatsuji, X. Li, M. Caricato, A. Marenich, J. Bloino, B. G. Janesko, R. Gomperts, B. Mennucci, H. P. Hratchian, J. V. Ortiz, A. F. Izmaylov, J. L. Sonnenberg, D. Williams-Young, F. Ding, F. Lipparini, F. Egidi, J. Goings, B. Peng, A. Petrone, T. Henderson, D. Ranasinghe, V. G. Zakrzewski, J. Gao, N. Rega, G. Zheng, W. Liang, M. Hada, M. Ehara, K. Toyota, R. Fukuda, J. Hasegawa, M. Ishida, T. Nakajima, Y. Honda, O. Kitao, H. Nakai, T. Vreven, K. Throssell, J. A. Montgomery, Jr., J. E. Peralta, F. Ogliaro, M. Bearpark, J. J. Heyd, E. Brothers, K. N. Kudin, V. N. Staroverov, T. Keith, R. Kobayashi, J. Normand, K. Raghavachari, A. Rendell, J. C. Burant, S. S. Iyengar, J. Tomasi, M. Cossi, J. M. Millam, M. Klene, C. Adamo, R. Cammi, J. W. Ochterski, R. L. Martin, K. Morokuma, O. Farkas, J. B. Foresman, and D. J. Fox, Gaussian, Inc., Wallingford CT, **2016**.

[2] C. Adamo, V. Barone, *J. Chem. Phys.* **1999**, *110*, 6158.

[3] F. Weigend, *Phys. Chem. Chem. Phys.* **2006**, *8*, 1057.

[4] S. Grimme, S. Ehrlich, L. Goerigk, *J. Comput. Chem.* **2011**, *32*, 1456.

[5] A. V. Marenich, C. J. Cramer, D. G. Truhlar, *J. Phys. Chem. B* **2009**, *113*, 6378.

[6] W. D. Cornell, P. Cieplak, C. I. Bayly, I. R. Gould, K. M. Merz, D. M. Ferguson, D. C. Spellmeyer, T. Fox, J. W. Caldwell, P. A. Kollman, *J. Am. Chem. Soc.* **1996**, *118*, 2309.

[7] a)J. Wang, W. Wang, P. Kollman, D. Case, *J. Mol. Graphics Modell.* **2006**, *25 2*, 247; b)J. Wang, R. M. Wolf, J. W. Caldwell, P. A. Kollman, D. A. Case, *J. Comput. Chem.* **2005**, *26*, 114.

[8] a)G. J. Martyna, D. J. Tobias, M. L. Klein, *J. Chem. Phys.* **1994**, *101*, 4177; b)M. Parrinello, A. Rahman, *J. Appl. Phys.* **1981**, *52*, 7182; c)M. E. Tuckerman, J. Alejandre, R. López-Rendón, A. L. Jochim, G. J. Martyna, *J. Phys. A: Math. Gen.* **2006**, *39*, 5629.

[9] N. Ehteshami, A. Eguia-Barrio, I. de Meatza, W. Porcher, E. Paillard, *J. Power Sources* **2018**, *397*, 52.

[10] H. Lee, T. Han, K. Y. Cho, M. H. Ryou, Y. M. Lee, *ACS Appl. Mater. Interfaces* **2016**, *8*, 21366.

[11] X. Zheng, T. Huang, Y. Pan, W. Wang, G. Fang, K. Ding, M. Wu, *ACS Appl. Mater. Interfaces* **2017**, *9*, 18758.

[12] H. Rong, M. Xu, B. Xie, W. Huang, X. Liao, L. Xing, W. Li, *J. Power Sources* **2015**, *274*, 1155.

[13] M. Hekmatfar, I. Hasa, R. Eghbal, D. V. Carvalho, A. Moretti, S. Passerini, *Adv. Mater. Interfaces* **2019**, *7*, 1901500.

[14] C. C. Su, M. He, C. Peebles, L. Zeng, A. Tornheim, C. Liao, L. Zhang, J. Wang, Y. Wang, Z. Zhang, *ACS Appl. Mater. Interfaces* **2017**, *9*, 30686.

[15] B. Liao, X. Hu, M. Xu, H. Li, L. Yu, W. Fan, L. Xing, Y. Liao, W. Li, *J. Phys. Chem. Lett.* **2018**, *9*, 3434.

[16] C.-C. Su, M. He, J. Shi, R. Amine, Z. Yu, L. Cheng, J. Guo, K. Amine, *Energy Environ. Sci.* **2021**, *14*, 3029.